



THIS MANUSCRIPT HAS BEEN SUBMITTED TO THE JOURNAL OF GLACIOLOGY AND HAS NOT BEEN PEER-REVIEWED.

Detection and Characterization of Discontinuous Motion on Thompson Glacier, Canadian High Arctic, Using Synthetic Aperture Radar Speckle Tracking and Ice-Flow Modeling

Journal:	<i>Journal of Glaciology</i>
Manuscript ID	JOG-23-0028.R1
Manuscript Type:	Article
Date Submitted by the Author:	n/a
Complete List of Authors:	Corti, Giovanni; Simon Fraser University, Earth Sciences Rabus, Bernhard; Simon Fraser University, Engineering Sciences Flowers, Gwenn; Simon Fraser University, Earth Sciences
Keywords:	Arctic glaciology, Remote sensing, Glacier modelling, Ice velocity, Glacier flow
Abstract:	<p>We investigate unusual discontinuous glacier motion on Thompson Glacier, Umingmat Nunaat, Arctic Canada, using synthetic aperture radar (SAR) images and ice-flow modeling. A novel intensity-rescaling scheme is developed to reduce errors in high resolution speckle tracking, resulting in a ~25% improvement in accuracy. Interferometric SAR (InSAR) and speckle tracking using high resolution RADARSAT-2 data indicate velocity discontinuities of up to 1 cm/day across deep and longitudinally extensive supraglacial channels on Thompson Glacier. We use a cross-sectional finite-element ice-flow model to determine the conditions under which velocity discontinuities of the observed magnitude and signature are possible. The modeling suggests that discontinuous motion across (long and straight) supraglacial channels can occur without ice fracture and under a wide variety of glacier thermal structures, including in fully temperate glaciers. Despite the wide range of conditions conducive to discontinuous motion, the form we observe requires that the associated channels be deep, longitudinally extensive and located in regions of lateral shearing. We speculate that these combined conditions are rare except on polythermal glaciers, where drainage features such as moulins are comparatively scarce and lower deformation rates allow channels to incise consistently and persist over many years.</p>



SCHOLARONE™
Manuscripts

Detection and characterization of discontinuous motion on Thompson Glacier, Canadian High Arctic, using synthetic aperture radar speckle tracking and ice-flow modeling

Giovanni CORTI,¹ Bernhard RABUS,² Gwenn E. FLOWERS¹

¹*Department of Earth Sciences, Simon Fraser University, Burnaby, BC, Canada*

²*Department of Engineering Sciences, Simon Fraser University, Burnaby, BC, Canada*

Correspondence: Giovanni Corti <gcorti@sfu.ca>

ABSTRACT. We investigate unusual discontinuous glacier motion on Thompson Glacier, Umingmat Nunaat, Arctic Canada, using synthetic aperture radar (SAR) images and ice-flow modeling. A novel intensity-rescaling scheme is developed to reduce errors in high resolution speckle tracking, resulting in a ~25% improvement in accuracy. Interferometric SAR (InSAR) and speckle tracking using high resolution RADARSAT-2 data indicate velocity discontinuities of up to 1 cm d^{-1} across deep and longitudinally extensive supraglacial channels on Thompson Glacier. We use a cross-sectional finite-element ice-flow model to determine the conditions under which velocity discontinuities of the observed magnitude and signature are possible. The modeling suggests that discontinuous motion across (long and straight) supraglacial channels can occur without ice fracture and under a wide variety of glacier thermal structures, including in fully temperate glaciers. Despite the wide range of conditions conducive to discontinuous motion, the form we observe requires that the associated channels be deep, longitudinally extensive and located in regions of lateral shearing. We speculate that these combined conditions are rare except on polythermal glaciers, where drainage features such as moulins are comparatively scarce and lower deformation rates allow channels to incise consistently and persist over many years.

27 INTRODUCTION

28 Over the last several decades, the resolution and availability of synthetic aperture radar (SAR) data
29 have increased dramatically (Ignatenko and others, 2020), creating new potential opportunities at the
30 intersection of glaciology and remote sensing (e.g., Yang and others, 2016). SAR, which was first applied
31 as a glaciological tool in 1993 to measure the velocities and grounding line positions of Antarctic ice streams
32 (Goldstein and others, 1993), allows for remote sensing of glacier motion regardless of daylight or weather
33 conditions (Joughin and others, 2011). Furthermore, as the radar is phase sensitive, interferometric SAR
34 (InSAR) techniques can be applied to resolve glacier motion at the centimeter scale, regardless of the
35 spatial resolution (essentially the pixel size) of the sensor (e.g., Goldstein and others, 1993; Gray and
36 others, 1998). Due to its accuracy, InSAR has been used to measure and investigate “mesoscale” glacier
37 phenomena that result in subtle (i.e., centimeter-scale) perturbations in surface ice velocity fields, such as
38 migration of subglacial water pockets (Fatland and Lingle, 2002) or movement of ice-shelf grounding lines
39 (Rignot, 1998; Rabus and Lang, 2002).

40 However, while InSAR delivers high resolution deformation measurements, it is only sensitive to motion
41 in the line-of-sight (LOS) direction of the radar and is plagued by a number of complex pitfalls stemming
42 from the cyclical nature of phase data (Yu and others, 2019). Thus, Gray and others (1998) introduced a
43 second SAR-based technique known as speckle tracking that avoids many of the InSAR pitfalls while also
44 measuring motion along both axes of the SAR image. However, unlike InSAR, the accuracy of SAR speckle
45 tracking is linked to the pixel size of the image (Gray and others, 2001; Bamler and others, 2009) and early
46 SAR sensors suffered from coarse spatial resolutions, with pixel sizes on the order of 10 m or larger. Thus,
47 for a number of years, researchers were often forced to choose between InSAR, which was directionally
48 limited and complex, or the simpler and more versatile, but much lower resolution, speckle tracking.

49 The spatial resolution of SAR sensors has increased significantly since the early 1990s, particularly
50 through introduction of sub-meter resolution spotlight modes, which now allow SAR speckle tracking to
51 approach the resolution of (regular, stripmap mode) InSAR. However, high resolution SAR speckle tracking,
52 which is able to resolve mesoscale glacier motion, remains a relatively under-exploited tool, generally only
53 being used to measure glacier- or ice-sheet-wide velocity fields, albeit at higher resolutions.

54 Spatially discontinuous glacier motion, which is poorly understood, in part due to a lack of observational
55 evidence, is one form of glacier motion that can now be measured using high resolution speckle tracking.

56 Discontinuous glacier motion generally results from the brittle failure and fracture of ice and can lead to
57 glacier velocity fields that are spatially or temporally discontinuous (e.g., serac fall or glacier collapse).
58 Discontinuous glacier motion also results in a variety of glacier structures such as crevasses and seracs and
59 can significantly contribute to glacier dynamics (Colgan and others, 2016; Faillettaz and others, 2015).

60 **Speckle tracking**

61 Single Look Complex (SLC) images, essentially SAR images with minimal processing applied post-focusing,
62 exhibit a characteristic speckle pattern. This speckle pattern is controlled by the roughness of the glacier
63 surface at the sub-pixel scale and can be tracked between SLCs, provided that the glacier surface remains
64 relatively unchanged (i.e., has non-zero interferometric coherence), as the speckle pattern is advected
65 downglacier (Moreira and others, 2013; Joughin, 2002). Speckle tracking itself is done by selecting a multi-
66 pixel chip of fixed shape from an initial SAR image and searching for a matching chip in a subsequent image
67 using the normalized two-dimensional (2-D) cross-correlation coefficient (NCC) as a similarity measure.
68 The NCC is generally calculated using the normalized product of SAR image intensities, but in some cases,
69 the interferometric phase is included and this then makes the similarity measure to be optimized equal
70 to the (intensity weighted) interferometric coherence (Joughin, 2002; Gray and others, 2001; Michel and
71 Rignot, 1999). In theory, for featureless areas, phase-based SAR speckle tracking is more accurate than its
72 intensity based counterpart, but is more computationally expensive and requires accounting for systemic
73 phase differences due to factors such as topography (Bamler and Eineder, 2005; De Zan, 2014). Thus, in
74 real-world scenarios, phase-based speckle tracking is used less frequently and may not outperform intensity
75 speckle tracking. It is important to note, however, that phase-based speckle tracking and intensity speckle
76 tracking are fundamentally linked, as a variation in coherence (i.e., decreases in complex cross-correlation
77 due to changing radar scatterers) will lead to corresponding differences of the speckle pattern between chips
78 as the spatial signature of the pattern is ultimately controlled by the phase and amplitude response of the
79 radar scatterers within the resolution cell.

80 A major benefit of SAR speckle tracking is that it is able to unambiguously resolve glacier motion
81 and benefits greatly from high resolution SAR images as its accuracy is directly linked to pixel size.
82 Moreover, the coherence (i.e., similarity resulting from an unchanged ground/glacier surface) of a scene
83 pair is often better preserved with high resolution SAR images (e.g., Mohammadimanesh and others, 2018)
84 as smaller pixels are less likely to capture an altered radar scatterer (Closson and Milisavljevic, 2017).

Corti and others:

85 Thus high resolution speckle tracking presents a powerful, but underleveraged, tool for investigating ice
86 dynamics associated with meso-glacier glacier motion. In this study, we develop an intensity prefilter for
87 SLCs designed to improve the performance of high resolution SAR speckle tracking and use this improved
88 method, in conjunction with a 2-D cross-sectional ice-flow model, to investigate unusual hypothesized
89 mesoscale discontinuous glacier motion on Thompson Glacier, Canadian High Arctic. Potential evidence
90 of this motion comes from preliminary InSAR analysis of the area that shows broken interferometric fringes,
91 a phenomenon that has previously been attributed to discontinuous motion (e.g., Kobayashi and others,
92 2018; Millan and others, 2022a; Rignot, 1996), albeit at much larger spatial scales.

93 **Study site**

94 The focus of this study, Thompson Glacier, is located at the head of Expedition Fjord on Umingmat
95 Nunaat (Axel Heiberg Island) in the Canadian Arctic Archipelago (Fig. 1). Thompson Glacier, the largest
96 of the Expedition Fjord glaciers, is an outlet glacier of the Mueller Ice Cap (Müller, 1962) and has several
97 named tributary glaciers including Piper (formerly Wreck) Glacier and Astro Glacier. While relatively
98 few glaciological studies have been conducted on Thompson Glacier, the neighboring White Glacier, which
99 is substantially smaller, is one of the most intensively studied (e.g., Hambrey and Müller, 1978; Blatter,
100 1987; Cogley and others, 1996; Thomson and others, 2017) glaciers in the Canadian Arctic largely due to its
101 proximity to the McGill Arctic Research Station (Thomson and Copland, 2017). Mapping of the Expedition
102 Fjord glaciers shows that, between 1948 and 1995, Thompson Glacier advanced approximately 950 m while
103 White Glacier retreated 250 m. The reason for this difference remains unclear, but researchers speculate
104 that differing response times to climatic forcings due to size differences or a slow surge on Thompson
105 Glacier may be responsible (Cogley and others, 2011).

106 A key feature of interest in this study is the large supraglacial channel on Thompson Glacier, which
107 we henceforth refer to as the Astro Channel, originating from Astro Lake and extending approximately
108 5 km down glacier. Preliminary remote sensing results indicate that discontinuous glacier motion may be
109 occurring around the Astro Channel, although the exact nature and cause of this hypothesized discontinu-
110 ous motion is unclear. A variety of observations over the last 75 years, beginning with aerial photography
111 in 1948 (photograph 60LT-72PL-C-8M219-72RS-11 AUG. 48-14C, National Archives of Canada), indicate
112 that the channel is a persistent feature. During field work conducted in the spring of 1961, Maag (1963)
113 observed the Astro Channel, noting that it drained Astro Lake and had depths of up to 30 m in some

114 areas. Researchers visiting the Astro Lake area in 1976 and 2008 photographed the Astro Channel, noting
 115 that the channel bridges over due to plastic deformation (swisseduc.ch/glaciers). Additionally, satellite
 116 imagery dating back to at least 2009 consistently shows the Astro Channel, although the degree to which
 117 it is bridged over varies.

118 REMOTE SENSING METHODS AND DATA

119 SAR data

120 We use SAR speckle tracking to measure the surface velocities of the Expedition Fjord area glaciers with
 121 a specific emphasis on the location near the Piper–Thompson confluence. SAR data used in this study
 122 (see Table S1 and Fig. S1) are collected with the spotlight beam mode of RADARSAT-2, a Canadian
 123 Space Agency SAR satellite with a 24-day repeat orbit, that operates at C-Band (5.6 cm wavelength) (Van
 124 Wychen and others, 2018; Morena and others, 2004). These SAR images have pixel sizes of 1.330–1.332 m
 125 in range and 0.379–0.414 m in azimuth. The spotlight beam mode itself employs electronic beam steering to
 126 dwell on the area of interest for a longer duration than would otherwise occur, resulting in the high image
 127 resolution in the satellite flight (i.e., azimuth) direction as compared to other imaging modes (MDA, 2018).
 128 The SAR data used in this study are only collected during the winter and spring as low temperatures
 129 and low snow accumulation help maintain glacier surface coherence, a prerequisite for accurate InSAR and
 130 SAR speckle tracking.

131 False matches due to high intensity pixels

132 Glacier speckle tracking results often contain rectilinear artifacts (see Fig. 2)—a geometry that suggest
 133 they are non-physical—due to the speckle tracking algorithm “locking-on” to various features. Here we
 134 investigate the underlying cause of these rectilinear artifacts and develop a compensating method to improve
 135 the accuracy of speckle tracking.

At its core, speckle tracking identifies similar areas in two consecutive SAR images using the *NCC*, which can be written

$$NCC = \frac{\sum_{x,y} [f(x,y) - \bar{f}_{x_0,y_0}] [g(x-x_0, y-y_0) - \bar{t}]}{\sqrt{\sum_{x,y} [f(x,y) - \bar{f}_{x_0,y_0}]^2 \sum_{x,y} [g(x-x_0, y-y_0) - \bar{t}]^2}}, \quad (1)$$

136 where $f(x,y)$ and $g(x,y)$ are the intensity values of the chips being compared, (x_0, y_0) represents the

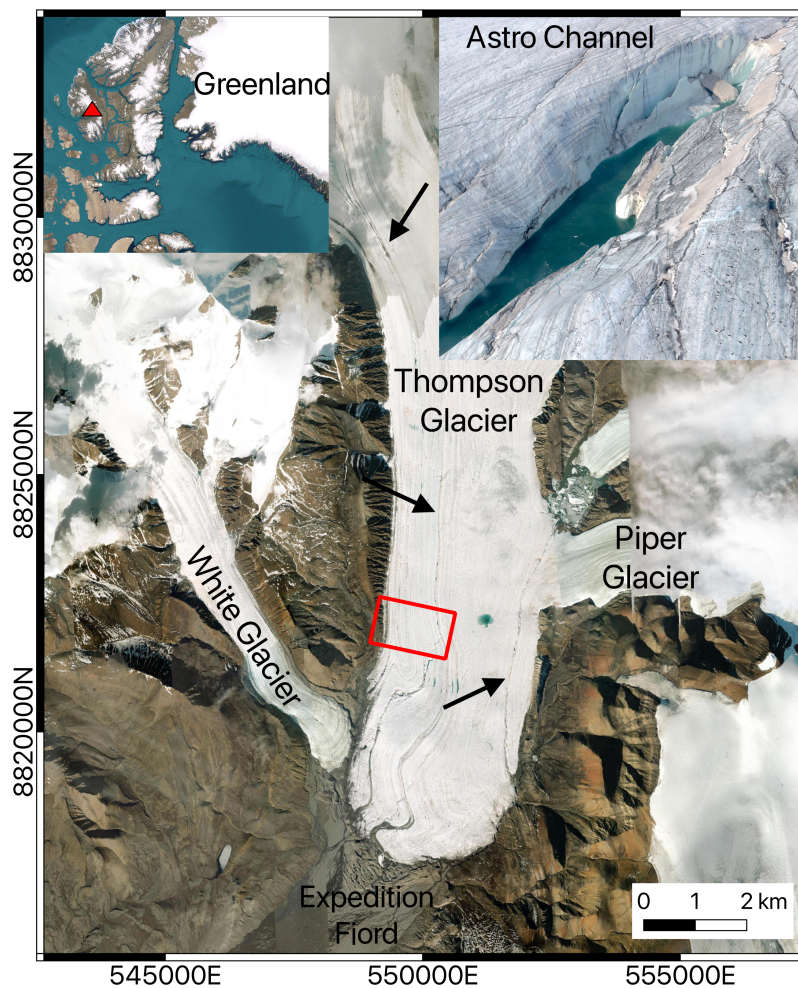


Fig. 1. Study site. Expedition Fjord glaciers on Umingmat Nunaat (Axel Heiberg Island), including Thompson Glacier, the subject of this study. The red box indicates the footprint used in developing the intensity rescaling scheme. The arrows indicate, from top to bottom, the Upper Channel, West Channel and Astro Channel across which discontinuous glacier motion is suspected to occur. Coordinates are given in UTM, Zone 15 N. The inset at top right shows the Astro Channel in 2022 near the Piper-Thompson Confluence. The photographer estimates the channel is roughly 10 m deep and 3 m wide. Astro Channel imagery courtesy of Laura Thomson and satellite imagery courtesy of Esri World Imagery (Esri, 2022).

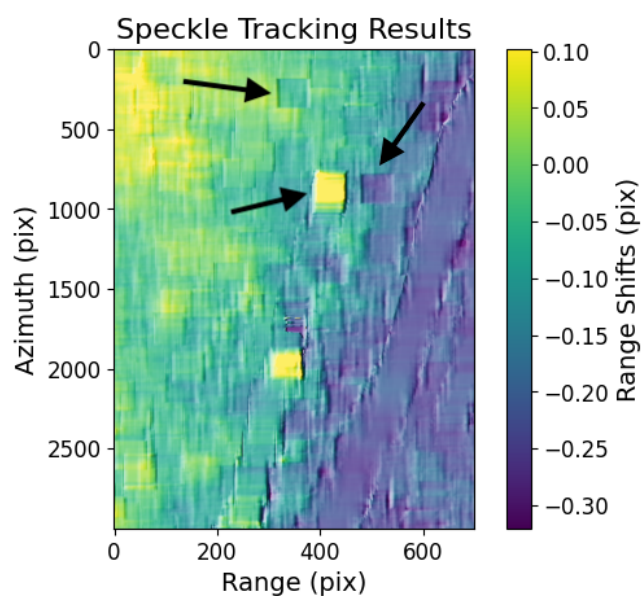


Fig. 2. Hillshaded (30× vertical exaggeration) SAR speckle tracking results (for range direction only) from SLCs collected on 5 January 2022 and 29 January 2022 over Thompson Glacier showing rectilinear “lock-on” artifacts. The arrows indicate several of the most obvious artifacts. As expected, the dimensions of these artifacts closely match the speckle tracking chip size, in this case 64×192 pixels in range and azimuth respectively. (see section on speckle tracking methods).

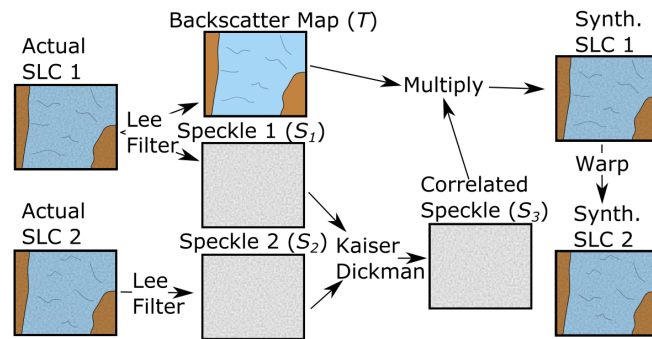


Fig. 3. Schematic outlining the process for generating the second synthetic SAR image used in the simulated SAR speckle tracking pair. Actual SLC 1 and synthetic SLC 2 will be used as the image pair.

coordinate translation between images, \bar{t} is the mean intensity of the selected chip and \bar{f}_{x_0, y_0} is the mean value of the region in $f(x, y)$ that is being searched (Yoo and Han, 2009). Equation (1) involves element-wise multiplication of the demeaned intensities of the two pixels in the same in-chip position. This makes the NCC particularly sensitive to situations in which high intensity pixels are in the same in-chip position, an issue that is compounded by the strong right-skew of a Rayleigh intensity distribution characteristic of a SAR image.

To reduce the prevalence of false matches caused by multiplication of high intensity pixels, we propose a non-linear intensity rescaling that will be applied to SAR images before speckle tracking to reduce the impact of high intensity pixels on the NCC .

146 Creating a simulated SAR image pair

To confirm that intensity rescaling can improve SAR speckle tracking performance, and to identify a rescaling that performs well, we develop a SAR simulator capable of producing a realistic glacier speckle tracking pair with a known motion field. We identify three key requirements for a realistic SLC pair: 1) a partially correlated speckle pattern, 2) a glaciologically realistic motion field and 3) realistic terrain (e.g., supraglacial streams, moraines, etc.) and speckle patterns. To generate a realistic SLC pair, we start with a real SAR image, covering a glacierized area, as the initial scene in the speckle tracking pair. For the second image, we use an SLC formed from a combination of speckle patterns, terrain maps and motion fields extracted from actual SAR images of the same glacierized area (see Fig. 3).

The process begins by selecting an area of interest (see Fig. 1) on Thompson Glacier that contains both the glacier margin, meaning that a significant velocity gradient will be captured, along with a large and

157 perennial supraglacial channel across which discontinuous glacier motion is suspected to occur. Both the
158 glacier margin and the channel provide clusters of high intensity pixels that may result in false speckle
159 tracking matches.

160 After selecting the area of interest, two (globally coregistered) SLCs are cropped to contain this common
161 area. The two images are chosen to maximize the temporal separation, and thus glacier surface change,
162 which results in the speckle patterns between them being as decorrelated as possible. The selected images
163 were acquired on 15 February 2018 and 22 May 2018, comprising the first and last SLCs available with
164 matching acquisition parameters. The SLC collected on 15 February 2018 will serve as the initial image in
165 the simulated speckle tracking scene pair.

166 A Lee sigma filter (Lee, 1983) with a 3×3 pixel window is used to obtain both the terrain backscatter
167 map, T (i.e., a speckle free image) and the speckle pattern S_1 from the initial real SLC. This filter, chosen
168 for its ease of implementation and low computational cost, is designed to suppress radar speckle while
169 preserving edges and fine details. A 3×3 pixel window is chosen in order to minimize blurring of surface
170 features in the terrain map. The same Lee sigma filter is also used to obtain S_2 , the speckle pattern from
171 the second real SLC. The major benefit of obtaining these speckle patterns from real data is that glacier
172 features such as marginal moraines will be captured in S_1 and S_2 if these features happen to exhibit some
173 control on the speckle patterns.

To form the second, simulated SLC in the speckle tracking pair, a speckle pattern that is partially
correlated with S_1 is necessary. This partial correlation simulates the minor changes in the glacier surface
that are inevitable over the 24-day repeat period of RADARSAT-2. S_3 , the speckle pattern for the sec-
ond simulated SLC, is formed by combining S_1 and S_2 using the Kaiser-Dickman algorithm (Kaiser and
Dickman, 1962):

$$S_3 = \rho S_1 + \sqrt{\rho - 1} S_2, \quad (2)$$

174 where ρ is the desired coherence. For our experiments, we chose $\rho = 0.8$, which results in a mean NCC of
175 0.543 for the simulated scene pair. This value is comparable to the mean NCC , for the same geographic
176 area, of the most coherent scene pairs used in this study and represents a realistic but favorable scenario
177 (i.e., little glacier surface change). To obtain the second SLC for the speckle tracking pair, S_3 is normalized
178 to unit mean to ensure it does not change the overall intensity of the second synthetic SLC and is then
179 multiplied element-wise by the terrain backscatter intensity map T (Xie and others, 2002).

180 A realistic glacier motion field is then introduced to the second simulated SLC using Lanzos resampling

Corti and others:

181 and a user-defined lookup table. The realistic glacier motion field itself is generated by taking the speckle
 182 tracking results from the 15 February 2018 and 11 March 2018 SLCs and smoothing the resulting motion
 183 field using a 20×60 pixel (approximately 30×30 m) boxcar filter.

184 Optimal intensity transformation

We begin by using the SAR simulator described above to test intensity transformations that follow

$$I_t = I^{(1/k)} \mid k \in \{1, 1.5, 2, 2.5, 3, 3.5\}, \quad (3)$$

185 where I represents the normalized intensities, achieved by dividing the original image by the mean intensity
 186 of the SLC. The range and step size of k is chosen to ensure that a minimum is captured and that there is
 187 a reasonable ($\sim 10\%$) difference in mean absolute error (MAE) between successive steps. $k = 1.5$ gives the
 188 best performing intensity transformation on the basis of MAE between the speckle tracking results and
 189 the imposed motion field. However, despite the measured MAE improvement, the speckle tracking results
 190 still pronounce outlier-type errors, appearing as rectilinear artifacts (e.g., Fig. 2), around the bright pixels
 191 that form the supraglacial channel in the simulated image pair. Thus, we test a piecewise transformation
 192 that applies a higher value of k , denoted k_h , to pixels above some intensity threshold. The piecewise
 193 transformation is given by

$$I_t = \begin{cases} I^{1/1.5} & I < t \\ I^{1/k_h} + (t^{1/1.5} - t^{1/k_h}) & I \geq t, \end{cases} \quad (4)$$

194 where t is a threshold intensity and the term $(t^{1/1.5} - t^{1/k_h})$ ensures that the piecewise function is
 195 continuous and monotonically increasing. A grid search with $k_h \in \{2, 3, 4, 5\}$ and $t \in \{1, 1.5, 2, 2.5, 3\}$ shows
 196 that $k_h = 3$, $t = 2$ yields the best performance with a MAE of 0.0477. This transformation represents a
 197 23% improvement over the untransformed case for the simulated speckle tracking pair.

198 Speckle tracking methods

199 To measure glacier motion, intensity-transformed speckle tracking is performed at the full image resolution
 200 (i.e., a one pixel step in both range and azimuth) using an upsampling factor of two and a 64×192 pixel
 201 correlation chip (prior to upsampling) in range and azimuth respectively. The chip size, which corresponds

202 to a ground footprint of approximately 80×80 m, is intended to be small enough to capture the glacier
203 motion of interest while still being large enough to provide robust matches. The upsampling factor is chosen
204 as a compromise between accuracy and computational cost (Magnard and others, 2017). A minimum cross
205 correlation threshold of 0.1 is used, where matches that fall below this threshold are discarded. The speckle
206 tracking itself is carried out using the GAMMA software's `offset_pwr_tracking` function.

207 Speckle tracking is only capable of measuring the glacier motion field in a 2-D plane defined by the range
208 and azimuth directions. To convert the measurements in this plane into glacier motion, we use the surface-
209 parallel flow assumption (e.g., Cumming and Zhang, 1999; Joughin and others, 2018) which assumes that
210 the true motion vector lies in the plane that is locally tangent to the glacier surface, equivalent to assuming
211 that emergence/submergence velocities are negligible over the temporal baseline of the speckle tracking
212 pair. In select cases, two speckle tracking results from substantially different look geometries overlap in
213 time and space, allowing for inversion of the full 3-D velocity field (e.g., Nagler and others, 2012; Wang and
214 others, 2019). ArcticDEM 7 (Porter and others, 2018) is used to define the locally tangent glacier surface
215 necessary for the surface-parallel assumption and for the geocoding used to align the two speckle results
216 employed in the 3-D velocity inversion.

217 For scenes of interest that contain the Astro Channel, where speckle tracking results indicate a sub-
218 stantial cross-channel velocity discontinuity, an additional masked speckle tracking is carried out. Here, ice
219 on each side of the channel is tracked separately (i.e., the other side is masked out) to ensure that speckle
220 tracking chips do not straddle the channel itself.

221 REMOTE SENSING RESULTS AND DISCUSSION

222 Intensity transformed speckle tracking is used to track glacier motion for the 30 scene pairs (see Table S1)
223 collected over the Expedition Fjord Area. In all cases, the scene pairs are formed from SLCs collected 24
224 days apart. Glacier speeds resulting from speckle tracking under the surface-parallel flow assumption (Fig.
225 4) match velocity data from NASA ITS_LIVE closely, with a mean absolute error of 0.52 cm d^{-1} . Note
226 that this comparison masks out ITS_LIVE velocities of less than 4 cm d^{-1} , as the underlying algorithm is
227 known to perform poorly in areas of slow-moving ice (Lei and others, 2021; Williams and others, 2021).

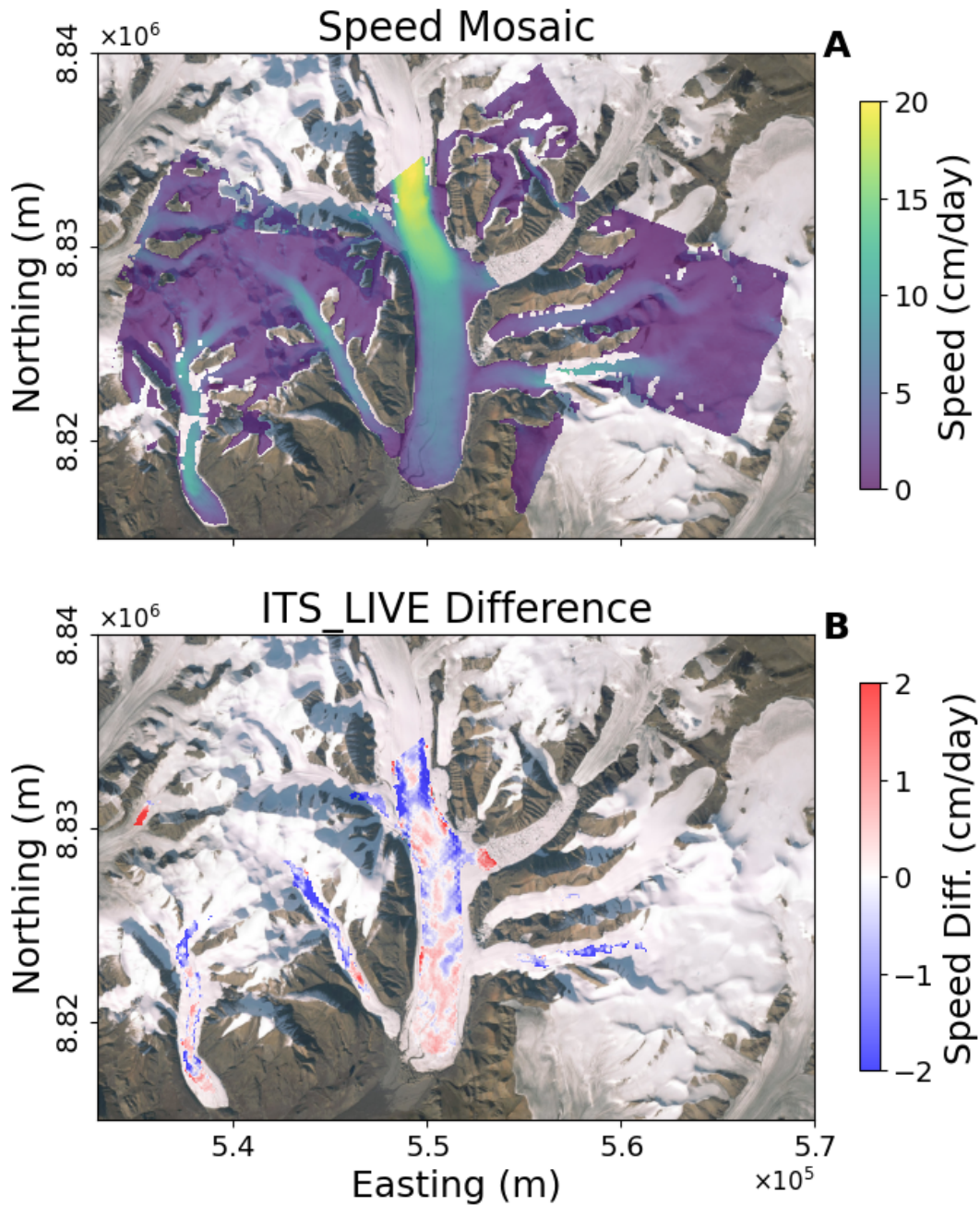


Fig. 4. Surface flow speed from SAR speckle tracking versus NASA ITS_LIVE data. (a) Average glacier speed as measured by speckle tracking under the surface parallel flow assumption and (b) Difference (ITS_LIVE-SAR) between NASA ITS_LIVE data and speckle tracking results. Note that the ITS_LIVE data are annual velocities whereas the speckle tracking data cover only winter and spring. ITS_LIVE velocity data are generated using auto-RIFT (Gardner and others, 2018) and provided by the NASA MEaSUREs ITS_LIVE project (Gardner and others, 2022). Optical imagery courtesy of Esri World Imagery (Esri, 2022).

228 **Broken fringes**

229 The glacier motion maps produced by SAR speckle tracking, along with ArcticDEM (Porter and others,
230 2018), are also used for InSAR analysis. We create interferograms sensitive only to glacier motion along
231 the satellite line-of-sight which show broken fringes in three different areas of Thompson Glacier. In all
232 three cases, the broken fringes align with large, persistent supraglacial channels that are visible in optical
233 satellite imagery dating back until at least 2009 and appearing in the same location in all RADARSAT-2
234 scenes used in this study which date from 2012, 2013, 2014, 2015, 2018 and 2022. Each channel appears
235 to be fed by an ice-marginal lake. We refer to these three channels as the Upper Channel, West Channel
236 and Astro Channel (see Fig. 1).

237 Broken InSAR fringes can be the result of 1) discontinuous motion, 2) a topographic discontinuity (i.e.,
238 a cliff or other steep topographic feature) that is not present in the DEM or 3) a topographic discontinuity
239 present in the DEM but that did not exist when the SAR data were collected. Mechanism 3 is easily ruled
240 out by examining the DEM, which contains no steep gradients in the areas of the broken fringes. Mechanism
241 2 can be investigated as fringe spacing resulting from topography would exhibit an inversely-proportional
242 stereo-like sensitivity to the spatial baseline (i.e., a measurement of the distance between the two acquisition
243 positions of the SAR satellite) of the scene pairs while fringes from motion fields would remain constant as
244 the spatial baseline changes (Pepe and Calò, 2017). Examination of consecutive interferograms with the
245 same acquisition parameters (e.g., Figs. 5, S2, S3), with baselines that vary by up to a factor of 4, show
246 highly consistent fringe patterns, indicating that the broken fringes result from persistent discontinuous
247 glacier motion.

248 It should be noted that a spatial discontinuity in the liquid water content of the snowpack may plausibly
249 cause broken interferometric fringes (Minchew and others, 2015). However, the extreme cold and thin Arctic
250 snowpack concurrent with many of the observed broken fringes preclude the presence of liquid water in the
251 snowpack. For example, from 15 February 2018 to 11 March 2018 (see Fig. 5), the maximum temperature
252 recorded at Eureka, the closest weather station located 120 km east of the study site at 100 m a.s.l., never
253 exceeded -18.9° C. Moreover, the aforementioned timeframe is not a special case as we almost exclusively
254 use SAR data collected during winter and early spring (i.e., low temperature periods) to avoid loss of
255 surface coherence due to melt.

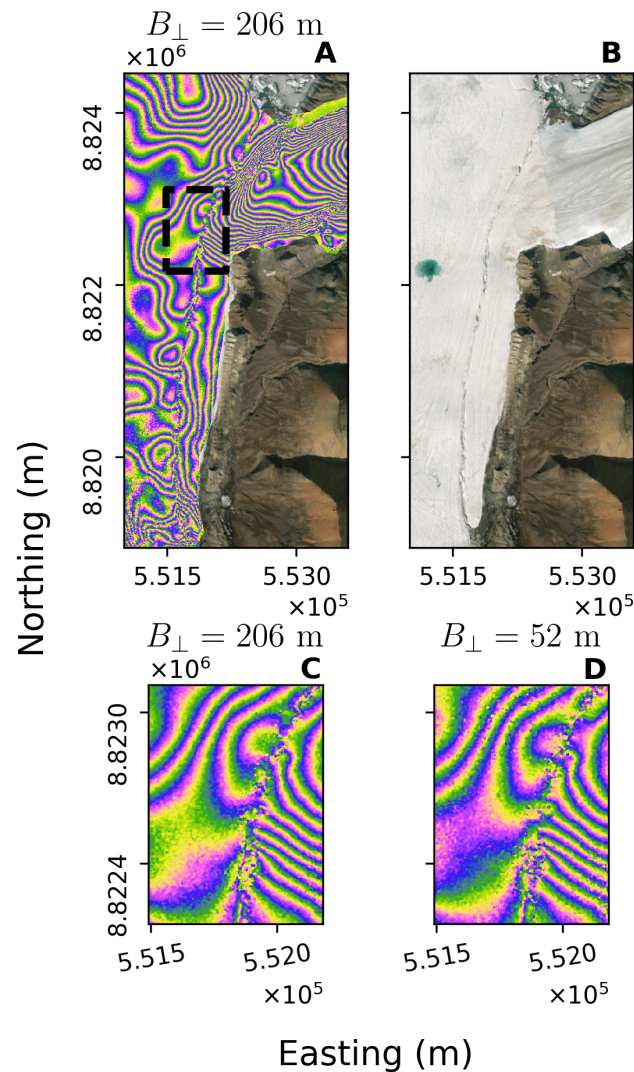


Fig. 5. Broken SAR interferometric fringes across the Astro Channel along with optical imagery. The interferogram in (a) and (c) is created using data from 15 February 2018 and 11 March 2018. The interferogram in (d) is created using data from 11 March 2018 and 4 April 2018. Panels (c–d) show a closeup of the respective interferogram in the area around the channel. Note that despite the significant difference in B_{\perp} , the magnitude of the fringe discontinuities is approximately equal in both interferograms, indicating discontinuous motion as opposed to discontinuous topography. Optical imagery courtesy of Esri World Imagery (Esri, 2022).

256 **3-D velocity profiles**

257 To characterize and visualize the Astro Channel discontinuity, we plot velocity profiles by sampling 3-D
258 velocity rasters across transects that run perpendicular to the channel. For each profile, velocities are
259 plotted from both the masked and unmasked 3-D inversion rasters. Fig. 6 shows these profiles for the 3-D
260 inversion results from the 29 January 2022 and 22 February 2022 (ascending) and 25 January 2022 and 18
261 February 2022 (descending) scene pairs which have the highest coherence of all the 3-D velocity inversions.
262 These velocity profiles show that while the magnitude of the velocity discontinuity varies from location
263 to location, the central (western) ice moves approximately 1 cm d^{-1} faster than the marginal (eastern)
264 ice. Velocity profiles are also plotted across the Upper and West channels (See Figs. S5 and S4) but no
265 discontinuous motion is visible in the resulting profiles, indicating that the discontinuous motion is too
266 small ($\lesssim 0.5 \text{ cm d}^{-1}$) to be resolved by speckle tracking.

267 As these profiles are sampled from the 3-D velocity rasters, it is also possible to separate the Easting,
268 Northing, Up (ENU) direction components of the discontinuous motion (Fig. 6f-i). Doing so shows that
269 the discontinuity is mainly ($>75\%$ in profiles 1 and 2) the result of differences in the north/south velocity
270 component, which is approximately aligned with the direction of the Astro Channel. This is noteworthy
271 as it means that the discontinuous motion along the Astro Channel is largely the result of differences in
272 ice velocity in the along-channel direction as opposed to differences in vertical velocities or some form of
273 overriding behavior similar, for example, to that observed at the confluence of Berendon Glacier (Eyles
274 and Rogerson, 1977).

275 **Temporal limitations**

276 The speckle tracking pairs used in this study are derived from SAR images collected during only winter
277 and spring in order to limit the temporal decorrelation caused by surface melt, and thus maximize the
278 accuracy of speckle tracking and InSAR. However, Thompson Glacier, like many polythermal glaciers,
279 likely exhibits seasonal velocity fluctuations (Thomson and Copland, 2017; Rabus and Echelmeyer, 1997)
280 characterized by increased velocities during the short melt season. No summer velocity measurements exist
281 for Thompson Glacier, but the neighboring White Glacier, which has velocity records dating back to the
282 1970s, shows summer velocity increases up to approximately 50% over winter velocities along a profile near
283 the glacier terminus (Thomson and Copland, 2017). On White Glacier, both the absolute and relative
284 magnitude of these summer velocity increases are greatest at a profile near the terminus and lower at an

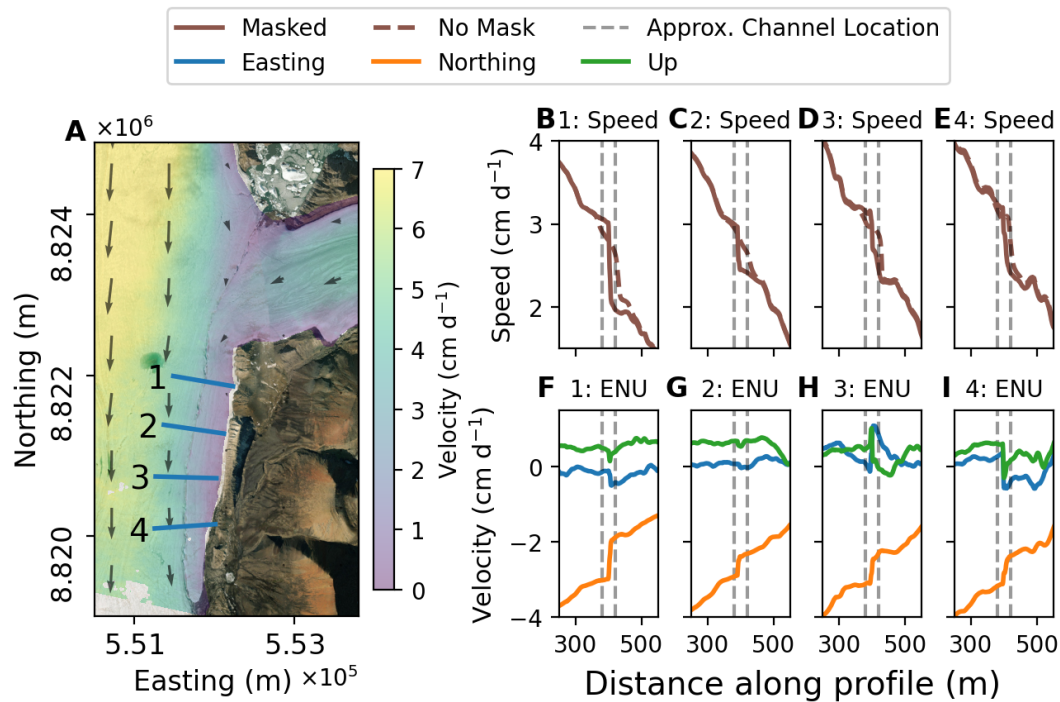


Fig. 6. 1-D profiles from 3-D inversion results from the 29 January 2022 and 22 February 2022 (ascending) and 25 January 2022 and 18 February 2022 (descending) scene pairs. (a) Location and number of each profile along with a velocity map. (b–e) The speed along each profile. Results for both the masked and non-masked SAR speckle tracking are shown as the dashed and solid brown lines respectively. (f–i) Profile velocity results, separated into ENU components. Note that the negative sign of the y-axis scale is the result of the ice largely moving south. The dashed black lines in (b–i) indicate the approximate location of the channel as obtained from manual delineation of the channel in optical satellite imagery. Optical imagery courtesy of Esri World Imagery (Esri, 2022).

285 upglacier profile. These summer velocity increases are likely caused by high basal water pressure which
286 leads to reduced friction at the glacier bed (Bingham and others, 2006; Thomson and Copland, 2017).

287 If a similar seasonal cycle occurs on Thompson Glacier, then the speckle tracking results presented here
288 do not capture this seasonal period of elevated glacier velocities. Thus the velocity maps presented in this
289 study should represent a slight underestimate of the annual glacier velocities, with the underestimate likely
290 being greatest near the glacier termini. Indeed, this may partially explain the spatial structure seen in Fig.
291 4b where the annual velocities from NASA ITS_LIVE data are generally greater than the SAR derived
292 velocities near the terminus. However, it should also be noted that the SAR speed mosaic (Fig. 4a) does
293 not account for emergence velocities and is largely derived from different time periods than the ITS_LIVE
294 data which, alternatively, may explain why the SAR-derived velocities are higher than the ITS_LIVE
295 velocities in some areas.

296 ICE-FLOW MODELING METHODS

297 We employ a two-dimensional cross-sectional ice-flow model in order to gain insight into possible causes
298 of the discontinuous glacier motion observed at the supraglacial stream channel originating from Astro
299 Lake (referred to as “the Astro Channel”). Specifically, the flow model is used to investigate the effects of
300 channel depth, sliding behavior and glacier thermal structure on the magnitude of a velocity discontinuity
301 across a cleft in a synthetic model domain inspired by the area of Thompson Glacier where the Astro
302 discontinuity is observed. It should be emphasized that this model is not intended to simulate Thompson
303 Glacier itself, as key information such as the bed profile, glacier thermal structure and even stream channel
304 depth are either unknown or poorly constrained. Instead, this model is intended to 1) investigate whether
305 a continuum (i.e., no ice fracture) model of glacier flow can produce velocity discontinuities comparable to
306 those observed and, if so, 2) quantify the effects of glacier and stream channel thermal structure, channel
307 depth and sliding behavior on the velocity discontinuity.

308 Model domain

309 The model domain (Fig. 7) represents a transverse cross section of a glacier that is 3 km wide and 425 m deep
310 at the center with a stream channel of some depth incised into the glacier surface 300 m from the eastern
311 margin. As the depth of the Astro Channel is uncertain, we use a number of different model domains with
312 varying stream channel depths. The bed profile is created by selecting several control points that are then

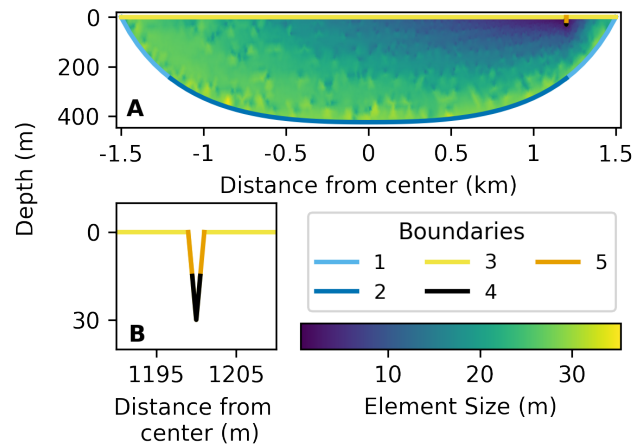


Fig. 7. The model domain for a channel depth of 30 m and a thermal transition location (L_t) 1200 m from center. (a) Model boundaries and element size, defined as the diameter of the circle that circumscribes the triangular element. 1.5 times vertical exaggeration. (b) Close up of the supraglacial stream boundaries. For the polythermal ice-flow models, boundary 1 is frozen to the bed, boundary 2 is either frozen to the bed or sliding according to a sliding-law coefficient and boundaries 3–5 are stress free. For the corresponding thermal models, a geothermal heat flux is applied along boundary 1, boundaries 2 and 5 have a heat flux of zero and boundaries 3 and 4 have a prescribed temperature based on plausible climatic conditions. These boundary conditions are described in greater detail in Table 1.

313 used to define a symmetrical basis spline curve that forms the bed profile. These control points, which
 314 consist of a depth and lateral position, are selected based on averages of the global ice thickness estimates
 315 (Farinotti and others, 2019; Millan and others, 2022b) in the study area. The glacier surface slope θ is
 316 approximated as 2.15° based on ArcticDEM (Porter and others, 2018). Each channel depth yields a slightly
 317 different model domain. All domains use second-order triangular Lagrange elements on a nonuniform grid
 318 and have $>15,900$ individual elements. Mesh refinement tests show that the solutions converge with the
 319 chosen mesh resolution to the same values as finer-mesh tests. The mesh itself is generated using the
 320 open-source mesh generator *gmsh* (Geuzaine and Remacle, 2009).

321 This model domain, and the associated boundaries in Fig. 7, are used to separately model both glacier
 322 thermal structure and ice flow. As no bed measurements exist for Thompson Glacier, we sometimes allow
 323 a possible basal thermal transition to occur between boundary 1 (frozen) and boundary 2 (temperate).
 324 The position of this boundary is permitted to vary within a 200 m horizontal range and a Weertman-type
 325 sliding law (Weertman, 1957) is introduced along boundary 2. In other cases, both boundaries 1 and 2 are
 326 frozen to the bed and no sliding occurs.

327 **Ice-flow equations**

We employ a steady state cross-sectional ice-flow model similar to those of Amundson and others (2006), Wilson and others (2013) and Armstrong and others (2016) in that our model captures lateral velocity gradients, is appropriate for the geometry of the study area and is computationally efficient enough to test a large set of model parameters. Following Nye (1965), we assume isotropic ice, no compression or extension in the flow direction and no vertical or transverse flow, thus reducing the ice-flow equation to

$$\frac{\partial}{\partial z} \left(\eta \frac{\partial u}{\partial z} \right) + \frac{\partial}{\partial y} \left(\eta \frac{\partial u}{\partial y} \right) = -\rho g \sin \theta. \quad (5)$$

Here, y and z are the transverse and vertical coordinates respectively, u is the velocity, ρ is the ice density, g is the acceleration due to gravity, θ is the ice-surface slope and η is the stress-dependent ice viscosity:

$$\eta = \frac{1}{2} A^{-1/n} \dot{\epsilon}_e^{-1+1/n}, \quad (6)$$

where A is the ice-creep parameter, $n = 3$ and the effective strain rate is written

$$\dot{\epsilon}_e = \frac{1}{2} \sqrt{\left(\frac{\partial u}{\partial z} \right)^2 + \left(\frac{\partial u}{\partial y} \right)^2}. \quad (7)$$

In some model configurations we use a Weertman-type sliding law (Weertman, 1957; Minchew and others, 2016), defined as

$$\tau_b = C u_b^{1/2}, \quad (8)$$

328 where τ_b is the basal shear stress, u_b is the basal velocity and C is the sliding-law coefficient, a constant
 329 related to basal friction. Given the absence of information about the bed of Thompson Glacier, the choice of
 330 sliding exponent—which matches that used in some previously published studies (e.g., Enderlin and others,
 331 2013)—is simply intended to yield physically plausible behavior along with reasonable computational cost
 332 and ease of implementation. In all cases considered here, at least some portion of the bed is assumed
 333 frozen, along which a no-slip ($u_b = 0$) Dirichlet boundary condition is imposed. In the sliding case $u_b = 0$
 334 is applied over boundary 1 and in the non-sliding case $u_b = 0$ is applied over boundaries 1 and 2. A
 335 no-stress Neumann boundary condition ($\nabla u = 0$) is prescribed along the glacier surface (boundaries 3, 4
 336 and 5).

337 The above equations are solved using **Firedrake**, an open source, finite-element package designed to
 338 solve partial differential equations (Rathgeber and others, 2016; Shapero and others, 2021). As the ice
 339 viscosity η is non-linearly dependent on the velocity field u , and the sliding law requires a Neumann
 340 boundary condition that is dependent on \sqrt{u} , an iterative method is used to solve for u . We use Picard
 341 iteration, in which an initial guess for u is supplied in order to calculate η , which is then used to calculate a
 342 new value of u . This process is repeated until the change in u between consecutive iterations is sufficiently
 343 small. For the purpose of Picard iteration, the difference between two consecutive velocity field solutions,
 344 u_k and u_{k+1} , is defined as the element-wise maximum absolute difference between u_k and u_{k+1} . For all
 345 model runs presented here, this difference threshold is set as 0.04 mm/day (1 mm/24 days), which is
 346 approximately 1/1000 of the central velocity of Thompson Glacier in the vicinity of the Astro Channel.

347 Thermal structure

Glacier thermal structures are generated by using **Firedrake** to solve a steady state heat diffusion equation under a variety of boundary conditions with internal heat sources. It should be stressed that this method is not intended to simulate the thermodynamic processes occurring in glaciers but rather to flexibly produce a variety of plausible glacier thermal structures that can be used to define the scalar field A (6). The diffusion equation is given by

$$\int_{\Omega} [k(T) \cdot \nabla(T) \cdot \nabla(w) - f_1(y) w] dx = 0, \quad (9)$$

348 where $k(T)$ is the thermal conductivity of ice, T is the temperature field and trial function, w is the test
 349 function, $f_1(y)$ is a piecewise, spatially varying heat flux, and Ω is the model domain (see supplementary
 350 materials for more details). The piecewise heat flux serves to slightly alter the thermal structure of the ice
 351 east of the channel, corresponding, in the real world, to the ice originating from Piper Glacier.

352 Along the upper surface of the glacier (boundary 3) and the bottom half of the channel (boundary 4),
 353 Dirichlet boundary conditions are applied where $T = T_s$ and $T = T_c$, respectively (see Table 1). Along
 354 the frozen bed margins (boundary 1), a heat flux of 40 mW m^{-2} is applied based on values reported at the
 355 toe of White Glacier (Blatter, 1987) and geothermal heat flux maps of the Canadian Arctic Basin (<https://www.cangea.ca/nunavutgeothermal.html>). Along the central bed (boundary 2), a temperature of
 356 either $T = -0.5^\circ\text{C}$ is prescribed in models with no sliding or the temperature is set to the pressure melting
 357 point (PMP) of pure ice if sliding is to occur. This PMP is calculated using only the ice overburden
 358

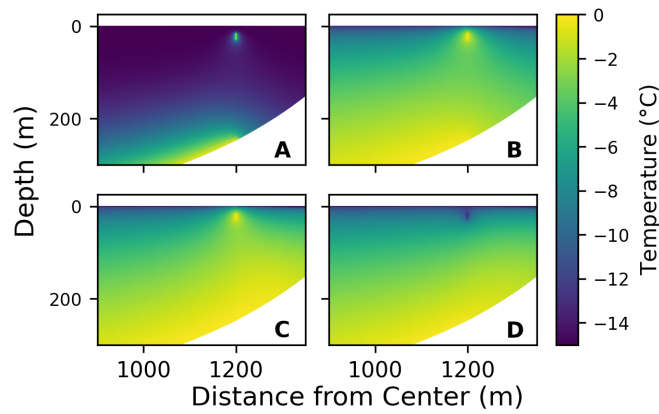


Fig. 8. Examples of generated thermal structures. Panel a) has $D_c = 30$ m, $T_s = -15^\circ\text{C}$, $T_c = 0^\circ\text{C}$, $F_t = 0$ mW m $^{-2}$, $G_t = 3$, $C = 1 \times 10^8$ Pa m s $^{-1}$ with each subsequent panel being identical to the previous except for one changed parameter. These changes are b) $G_t = 1/3$ c) $F_t = 2/1500$ mW m $^{-2}$ d) $T_c = -15^\circ\text{C}$.

359 pressure, as the model assumes no compression or extension along the flowline. Finally, to prevent numerical
 360 instabilities that occur in the presence of steep temperature gradients due to low surface temperatures
 361 (boundary 3) and high channel temperatures (boundaries 4 and 5), a no-heat-flux boundary condition is
 362 prescribed over boundary 5.

Solving the heat equation under the conditions outlined above yields a uniform vertical temperature gradient in ice unaffected by the tributary (f_1) and geothermal (boundary 1) heat fluxes. In order to generate variable vertical temperature gradients, as are usually observed in glaciers, a non-linear rescaling is applied to the temperature fields after their initial generation. This rescaling preserves the minimum and maximum temperature values and is given by

$$T = (T_{\max} - T_{\min}) \times \left(\frac{T - T_{\min}}{T_{\max} - T_{\min}} \right)^{G_t} + T_{\min}, \quad (10)$$

363 where T is temperature, T_{\max} (T_{\min}) is the maximum (minimum) value in the temperature field and G_t is
 364 the temperature gradient factor. Ice temperatures exceeding the PMP are clipped at this value.

The resulting temperature fields (see Fig. 8 for examples) are then converted into ice viscosity values for use in the ice-flow model. According to Cuffey and Paterson (2010), the relationship between the ice temperature T ($^\circ\text{C}$) and A is given by

$$A = A_* \exp\left(-\frac{Q_c}{R} \left[\frac{1}{T_h} - \frac{1}{T_*} \right]\right), \quad (11)$$

Corti and others:

365 where $A_* = 3.5 \times 10^{-25} \text{ Pa}^{-3} \text{ s}^{-1}$ is the value of A at -10°C , $T_* = 263 + 7 \times 10^{-8}P$, $T_h = T + 7 \times 10^{-8}P$,
 366 P is the pressure and

$$Q_c = \begin{cases} Q^- = 6 \times 10^4 \text{ J mol}^{-1} & T_h < T_* \\ Q^+ = 11.5 \times 10^4 \text{ J mol}^{-1} & T_h > T_* \end{cases} \quad (12)$$

367 As (5) assumes no compression or extension in the x or y directions (Nye, 1965) we set $P = -z \rho g$, the
 368 ice overburden pressure where $-z$ is the depth within the glacier and $\rho = 917 \text{ kg m}^{-3}$, the density of pure
 369 ice.

370 Model parameters

371 We aim to select a set of model parameters that result in thermal structures, channel depths and sliding
 372 behaviors that cover the range of plausible scenarios for Thompson Glacier. In some cases, model parame-
 373 ters that fall outside the plausible range for Thompson Glacier are selected as they may provide insight into
 374 the general phenomenon of discontinuous motion across a channel. The selected set of model parameters
 375 are reviewed below and summarized in Table 1. Note that all selected parameter combinations were tested
 376 and included in the model analysis except for those that exhibit numerical instabilities.

377 The selected glacier surface temperatures (T_s) range from -10°C to -20°C , a range based on mean
 378 annual air temperatures in the Canadian High Arctic and in the vicinity of the study area. Channel
 379 temperatures (T_c) range between the glacier surface temperature and 0°C , which represents water flowing
 380 in the channel. Additionally, to represent the possibility of cold-air pooling in the channel, a value of T_c
 381 2 K below T_s is tested. Modeled channel depths extend to 30 m, which is the maximum supported by
 382 field observations (Maag, 1963). Small heat fluxes (F_t), resulting in a temperature variation of $\pm 2 \text{ K}$, are
 383 prescribed in the ice east of the channel, corresponding, in the real-world, to ice originating from Piper
 384 Glacier. Non-physical temperature gradient factors (G_t) are introduced to mimic non-linear temperature-
 385 depth gradients as are found in many glaciers. We test factors that give both concave up and concave down
 386 temperature-depth profiles. Values of C , which describe the basal friction, are selected to give a wide range
 387 of sliding ratios while resulting in realistic sliding speeds. A zero sliding case is also included in our tests.
 388 Finally, the thermal transition location (L_t), in other words, the lateral position of the basal slip-to-no-slip
 389 transition that occurs at the intersection of the frozen margin and the thawed bed, is allowed to vary from
 390 the lateral position of the channel by up to $\pm 100 \text{ m}$ in each direction. Further justification for the model

Symbol	Description	Location	Values	Units
T_s	Temperature	Glacier surface	$[-10, -12.5, -15, -17.5, -20]$	$^{\circ}\text{C}$
T_c	Temperature	Channel	$[0, -5, -10, T_s - 2, T_s]$	$^{\circ}\text{C}$
D_c	Channel depth	Channel	$[10, 12.5, 15, 17.5, 20, 22.5, 27.5, 30]$	m
F_t	Heat flux	Tributary ice	$[-2/1550, -1/1550, 0, 1/1550, 2/1550]$	mW m^{-2}
G_t	Temperature gradient factor	Everywhere	$[1/3, 1/2, 1, 2, 3]$	1
C	Sliding-law coefficient	Central bed	$[1 \times 10^8, 3.5 \times 10^8, 7 \times 10^8, \text{None}]$	$\text{Pa m}^{-1/2} \text{ s}^{1/2}$
L_t	Thermal transition location	Frozen margin	$[1100, 1150, 1200, 1250, 1300]$	m

Table 1. Parameters used to generate glacier thermal structure, model domain and sliding behaviour. Note that channel depth (D_c) is the only parameter that alters the model domain and that the values used to describe L_t correspond to the coordinate system shown in Fig. 7.

parameter selections are given in the supplementary material.

Temperate glaciers

As a point of comparison, we model a set of temperate glaciers with varying channel depths and sliding behaviors. For these temperate glaciers, the same bed profile is used and the ice temperature is chosen to be at the PMP everywhere. A Dirichlet boundary condition of $u_b = 0$ is prescribed along a 1 m swath of the bed at the outermost edges of the glacier domain. This is done as, for (5), a Dirichlet boundary condition must be prescribed somewhere or the velocity field can only be determined up to a constant. Note that this will not alter the metrics we use to measure the discontinuity as both are unaffected by any constant velocity offset. We model two end-member types of sliding behavior: a high slip case ($C = 1.0 \times 10^8 \text{ Pa m}^{-1/2} \text{ s}^{1/2}$) and a no-slip case ($u_b = 0$ for the entire bed). Sliding is calculated using the same Weertman-type sliding (8) law employed in the polythermal glacier modeling. The no-sliding case is not physically realistic for temperate glaciers but does provide a useful lower bound for low slip beds.

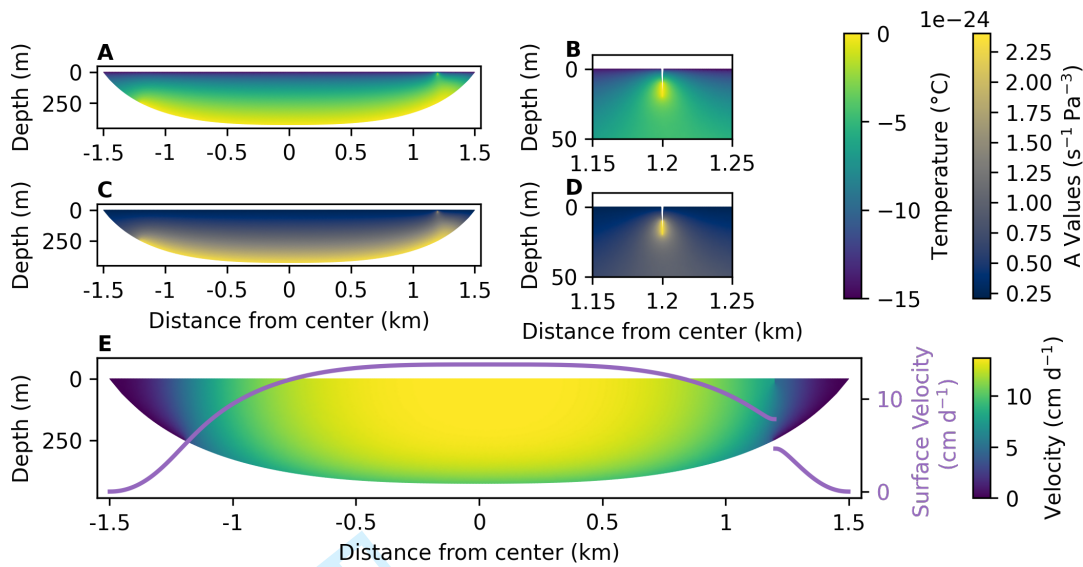


Fig. 9. Model results for $T_s = -15^\circ\text{C}$, $T_c = 0^\circ\text{C}$, $D_c = 20\text{ m}$, $F_t = 2/1550\text{ mW m}^{-2}$, $G_t = 1/2$, $C = 3 \times 10^8\text{ Pa m s}^{-1}$ (see Table 1). (a) Temperature. (b) Close-up of (a). (c) Flow-law coefficient A . (d) Close-up of (c). (e) Velocity field and surface velocity.

403 ICE-FLOW MODELING RESULTS AND DISCUSSION

404 Polythermal glaciers

405 We model 134,758 numerically stable simulations with unique combinations of glacier thermal structures,
 406 channel depths and sliding behaviors. Fig. 9 shows examples of spatially distributed model outputs,
 407 including glacier temperatures, the corresponding values of A and glacier velocities. For each model run,
 408 the surface velocity on either side of the channel, the central surface velocity and central basal velocity are
 409 output. A non-dimensional discontinuity fraction, defined as the magnitude of the discontinuity divided
 410 by the velocity range of the glacier, is computed as a metric of discontinuity size relative to the overall
 411 glacier velocity (Fig. 10h–j).

412 The velocity range, as opposed to the velocity maximum, is used in calculating the discontinuity fraction
 413 as it removes any component of plug flow, thus allowing a direct comparison between polythermal and
 414 temperate glacier simulations. For the polythermal glaciers discussed here, the velocity range is equivalent
 415 to the maximum velocity and using the velocity range has no effect on the discontinuity fraction.

416 The modeled glaciers produce discontinuity fractions ranging from 0.040 to 0.370 with a mean of 0.137
 417 (Fig. 10). For reference, the observed discontinuity fraction across Astro Channel is approximately 0.13.
 418 These fairly substantial discontinuity fractions are, themselves, a key result. They demonstrate that it is

419 possible to achieve non-negligible discontinuous surface velocity fields such as those observed across the
420 Astro Channel in the absence of ice fracture or highly specific thermal structures or sliding behaviors. The
421 occurrence of cross-channel velocity discontinuities in the absence of ice fracture is in line with other work
422 (e.g., Moore and others, 2010; Monz and others, 2022) that casts doubt on ice fracture being responsible
423 for structures attributed to thrust faulting. Indeed, the modeling shows that a fairly wide range of thermal
424 structures and channel depths should give rise to discontinuous velocity fields detectable by high resolution
425 remote sensing.

426 Several factors related to the discontinuity fraction distributions shown in Fig. 10a–g should be noted.
427 First, channel depth is the only single variable that has a strong control on both the minimum and maximum
428 discontinuity fraction. With all other variables, the maximum discontinuity fraction may change with
429 variable choice but the minimum discontinuity fraction remains close to zero. This change in maxima only
430 is most pronounced for the channel temperature, in which cold channels limit the maximum discontinuity
431 fraction more strongly than their warm counterparts. A similar, albeit weaker, phenomenon occurs with
432 the bed friction parameter C , surface temperature and temperature gradient factor.

433 **Temperate glaciers**

434 We model temperate glaciers with channel depths of D_c (see Table 1). For each channel depth, the
435 temperate discontinuity fractions (see Fig. 10a) closely bound ($\leq \pm 16\%$) the smallest polythermal fractions
436 for corresponding channel depths, while the temperate magnitudes (See Fig. S6) exceed the median of their
437 polythermal counterparts by at least 20%. However, the smaller temperate discontinuity fractions are due
438 to the comparatively large surface velocities of the temperate glaciers, as opposed to small cross-channel
439 velocity discontinuities.

440 **Model limitations**

441 The cross-sectional nature of the ice-flow model discussed above results in several shortcomings, notably
442 it neglects the longitudinal compression that results in measurable emergence velocities and inherently
443 assumes that the glacier geometry (including the supraglacial channel) and thermal structure are longitu-
444 dinally uniform. These geometric assumptions imply that the modeled supraglacial channel is infinitely
445 long and perfectly straight, resulting in a discontinuity maximizing scenario as compared to channels that
446 exhibit overall curvature or sinuosity. While channel curvature or sinuosity should reduce the discontinuity

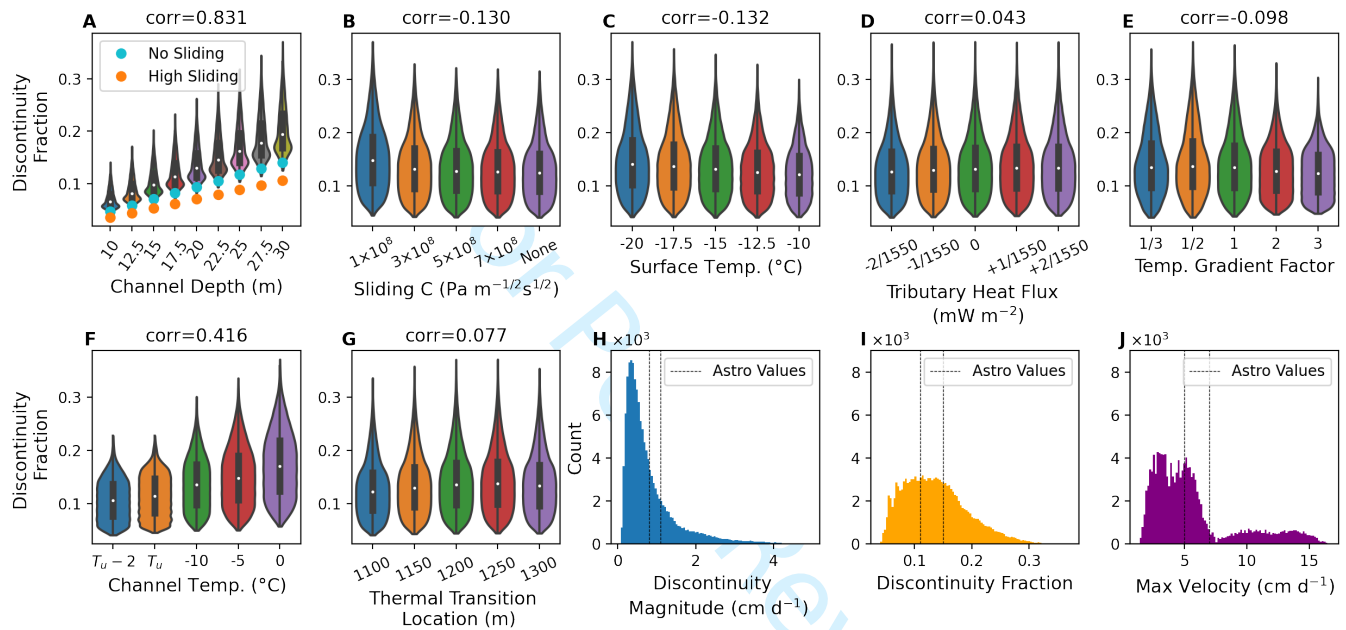


Fig. 10. Violin plots (a–g) for each model parameter in Table 1 and histograms (h–j) for all model results. Violin plots include Spearman correlation scores for discontinuity fraction and parameter along with a box plot showing the mean (white dot) and inter-quartile range (thick black bar). Panel (a) includes discontinuity fraction for the temperate glaciers with varying channel depths and sliding behaviors (orange and blue dots). For the high sliding case $C = 1.0 \times 10^8 \text{ Pa m}^{-1/2} \text{ s}^{1/2}$. Dashed black lines in (h–j) indicate the approximate range of values observed at the Astro discontinuity.

447 magnitude for a given set of model parameters, it is unclear how substantial the impact will be.

448 However, the largest shortcoming of the ice-flow model used above is not related to its cross-sectional
449 nature but instead results from the lack of thermomechanical coupling. For the modeled glaciers, the thermal
450 structure is simply generated by solving a heat diffusion equation over the model domain using boundary
451 conditions that are loosely based on the climate of the study site. This method of generating thermal
452 structures greatly reduces the complexity and computational cost of the model but fails to account for
453 the thermal effects of ice advection and strain heating. A key result of the missing advection is that the
454 temperature gradient with depth resulting from the heat diffusion equation is always linear and must be
455 rescaled with a temperature gradient factor in order to achieve the depth-varying temperature gradients
456 found in real glaciers. The lack of strain heating will impact the thermal structure, and thus the velocity
457 field, throughout the glacier. At the discontinuity itself, where deformation rates are quite high, lack of
458 strain heating and its ice softening effects may cause the model to underestimate the magnitude of the
459 velocity discontinuity when compared to a thermomechanically coupled model. However, rough estimates
460 show that the influence of strain heating is much too small to cause any potential positive feedback loop
461 that may lead to thermomechanical-runaway. For the fastest modeled (i.e., highest slip) glaciers here,
462 maximum strain heating rates are $\sim 4000 \text{ J m}^{-3} \text{ d}^{-1}$, and only occur in a small volume directly beneath the
463 channel. This energy is sufficient to melt $\sim 14 \text{ g m}^{-3}$ of temperate ice, leading to a negligible increase in
464 interstitial water, and thus negligible changes in A .

465 While the lack of thermomechanical coupling yields less accurate glacier velocity fields, the simplicity and
466 therefore low computational cost of the model allows for testing a large number of model configurations.
467 The large parameter space explored is useful, as many important model parameters such as channel depth,
468 surface temperature and channel temperature are either unknown or poorly constrained. Moreover, as the
469 modeling is intended to give a general understanding of ice flow across large supraglacial stream channels,
470 the additional accuracy gained from thermomechanical coupling is not essential to the interpretation of model
471 results.

472 **Additional controls on A**

473 Finally, we do not explicitly consider the possibility of water intrusion or strong single maximum fabrics
474 in the ice around the channel. Both of these factors can substantially alter A (Jacka and Budd, 1989;
475 Adams and others, 2021; Duval, 1977) and may plausibly occur around water-filled supraglacial channels

Corti and others:

476 in areas undergoing high shear, such as the Astro Channel. Both interstitial water content and strong
477 single maximum fabrics in simple shear should only serve to increase A , leading to a similar qualitative
478 effect as high channel temperatures (i.e., an increase in discontinuity magnitude). As a point of reference,
479 strong single maximum fabrics can result in an increase in A by up to a factor of 9 (Jacka and Budd, 1989;
480 Jun and others, 1996), an impact similar to increasing ice temperature from -12.5°C to 0°C . Similarly, an
481 increase in interstitial water content from zero to 1.1% will lead to a three-fold increase in the value of A
482 (Duval, 1977). Such values exceed those included in our model.

483 DISCUSSION

484 Discontinuity causing channel geometry

485 The modeling results indicate that cross-channel velocity discontinuities substantial enough to be measured
486 by high resolution remote sensing or in-situ methods can occur under a wide variety of thermal conditions
487 (including in temperate glaciers) and sliding behaviors, and do not require implausibly deep supraglacial
488 channels. However, observations of these cross-channel velocity discontinuities remain rare to date. The
489 lack of observations likely occurs for two reasons. First, researchers are simply not measuring velocity fields
490 across supraglacial channels using in-situ methods. In addition, remote sensing that happens to image areas
491 in which cross-channel velocity discontinuities occur will likely be unable to resolve the discontinuities unless
492 a high resolution sensor is used. The sensor resolution necessary to detect a cross-channel discontinuity
493 will depend on the temporal baseline and discontinuity magnitude, but a sensor capable of resolving
494 glacier motion of $\sim 1\text{ cm d}^{-1}$ is a reasonable estimate. Furthermore, significant spatial smoothing, which
495 is commonly performed on remotely sensed glacier velocity fields, will likely obscure any discontinuous
496 motion.

497 Second, and more importantly, for supraglacial channels to form discontinuous motion fields, specific
498 geometric requirements must be met. As the local transverse velocity gradient is proportional to the
499 discontinuity fraction and magnitude (see Fig. S7), the channel must be positioned in a region of substantial
500 lateral velocity gradients (and thus shear stresses) that are sustained over fairly long (likely kilometer-scale)
501 distances. This means that the channel must be long and located in a band near the glacier margin where
502 high shear stresses occur and run approximately parallel to the glacier flow direction. Channel depth also
503 plays an important role, with model results indicating that as channels become shallower, an increasingly
504 small number of parameter combinations give rise to substantial discontinuities. Defining a depth threshold

505 for substantial discontinuous motion would require knowledge of glacier-specific properties such as thermal
506 structure and sliding behavior. Supraglacial channels that meet these length and position criteria appear
507 uncommon, but are more likely to occur on polythermal glaciers, which tend to have fewer drainage features
508 such as moulins compared to their temperate counterparts (Bingham and others, 2003) and thus longer
509 supraglacial streams and channels.

510 Moreover, to form channels of sufficient depth, very high incision rates or perennial occupation by
511 meltwater are necessary. On polythermal glaciers, perennial occupation by meltwater appears necessary
512 as anomalously high incision rates compared to those that have been observed would be necessary to form
513 channels of 10+ m depth in a single melt season (St Germain and Moorman, 2019; Irvine-Fynn and others,
514 2011). On temperate glaciers, where incision rates are generally higher than those found on polythermal
515 glaciers, even when compared to the local ablation rates, it may be possible to form sufficiently deep
516 channels in a single melt season with very high but still plausible incision rates (Isenko and others, 2005;
517 Ferguson, 1973). However, some research indicates that the high discharge rates necessary to cut these
518 channels in temperate glaciers are correlated with high sinuosity which would likely inhibit the velocity
519 discontinuity by reducing the longitudinally averaged channel depth (St Germain and Moorman, 2019;
520 Ferguson, 1973). Perennially occupied supraglacial channels, which may result in deep channels with
521 lower sinuosity due to their lower discharge rates, are unlikely to form on temperate glaciers as high
522 deformation rates would close the channel between melt seasons (Hambrey, 1977; Irvine-Fynn and others,
523 2011). Alternatively, if a velocity discontinuity across a sinuous supraglacial channel does occur, the
524 differential motion may cause the channel to pinch itself shut as one bank of the channel migrates into the
525 other, provided the velocity discontinuity is greater than the rate at which the stream incises into the ice.
526 In sum, the probability of a supraglacial channel meeting the length, depth and direction criteria necessary
527 to cause a surface velocity discontinuity are small, with the most likely scenario occurring when perennial
528 supraglacial streams form on polythermal glaciers.

529 **Thompson Glacier channels**

530 All three channels (i.e., Astro, West and Upper channels) on Thompson Glacier at which interferograms
531 indicate the presence of discontinuous motion appear to match the length, depth and direction criteria
532 to a degree. These three channels are large enough to appear prominently in satellite imagery, likely
533 indicating that they are at least several meters deep although the Astro Channel appears wider, and thus

Corti and others:

534 probably deeper, than the Upper and West channels. All three channels are also approximately aligned
535 with the direction of glacier flow for 2+ km. In the case of the Upper Channel, the distance from the
536 glacier margin is approximately 400 m, similar to that of the Astro Channel, with the transverse velocity
537 gradients, as measured by speckle tracking, being approximately twice as large as those in the vicinity
538 of the Astro Channel. However, speckle tracking is unable to resolve a velocity discontinuity across the
539 Upper Channel, indicating a cross-channel velocity difference of $\lesssim 0.5 \text{ cm d}^{-1}$. This comparatively small
540 velocity discontinuity, despite the larger transverse velocity gradient, is most easily explained as the result
541 of a shallower channel depth. The West Channel is located approximately 900 m from the glacier margin,
542 with transverse velocity gradients that are $\sim 10\%$ of those at the Astro Channel. Again, speckle tracking is
543 unable to resolve a velocity discontinuity across this channel, indicating a cross-channel velocity difference
544 of $\lesssim 0.5 \text{ cm d}^{-1}$. This comparatively small velocity discontinuity could result from a combination of low
545 shear stresses across the West Channel, as indicated by the transverse velocity gradients, and shallower
546 channel depths.

547 **Controls on channel formation and geometry**

548 The three supraglacial channels on Thompson Glacier where discontinuous motion is detected originate
549 at glacier confluences and are fed by marginal lakes, likely indicating meltwater occupation for part of
550 the year. We speculate that channels conducive to discontinuous glacier motion may form preferentially
551 at glacier confluences due to structural controls imposed by the two flow units. From optical satellite
552 imagery we discern, qualitatively, that many glaciers on Umingmat Nunaat (Axel Heiberg Island) have
553 long, flow-parallel supraglacial channels that originate at glacier confluences. Some, but not all, of these
554 channels appear to be fed by ice-marginal lakes. Relatively little is known about what controls the location
555 of supraglacial stream formation, however Hambrey (1977) has suggested that glacier structures, including
556 flow units, may play some role in determining the location of small supraglacial streams. Moreover,
557 Hambrey (1977) observed that many of these small streams follow structural features and, as a result, are
558 often fairly straight. At a glacier confluence troughs may form between the two flow units (Glasser and
559 Gudmundsson, 2012) which could create a structural feature that may potentially be exploited by water
560 to form a long, flow-flowing supraglacial stream. Any shearing that occurs between two flow units will
561 serve to preferentially align existing surface features, including supraglacial channels or troughs, with the
562 flow direction. This, combined with the fact that asymmetric glacier (i.e., glaciers of mismatched size)

563 confluences are likely to form a zone of high shear, may preferentially lead to formation and persistence of
564 channels, located in zones of high shear, that have geometries conducive to discontinuous glacier motion.

565 The bed topography presents another potential control on channel formation. We do not model such
566 scenarios owing to limited information about the bed of Thompson Glacier, but the most relevant scenario
567 here would be a topographic step underlying the Astro Channel. Such a step could potentially fix the
568 location of a slip-to-no-slip transition at the bed which may then cause preferential erosion under the
569 thawed central portion of the bed (Cook and others, 2020), leading to an increase in step size. If such
570 a step exists, the sharp difference in ice thickness and thermal structure across the Astro Channel would
571 likely increase the size of any velocity discontinuity for a given set of parameters.

572 CONCLUSION

573 High resolution SAR speckle tracking of glaciers remains largely underleveraged but may be broadly useful
574 to measure and investigate mesoscale (multi-centimeter) glacier motion. In this study, we use high reso-
575 lution speckle tracking to investigate mesoscale discontinuous motion, initially detected by InSAR, across
576 supraglacial stream channels on Thompson Glacier, Umingmat Nunaat (Axel Heiberg Island). To improve
577 the accuracy of our speckle tracking, we develop and use an intensity prefilter designed to reduce false
578 matches. We then use a 2D cross-sectional ice-flow model to investigate the controls on discontinuous
579 glacier motion similar to that observed on Thompson Glacier.

580 As the magnitude of the velocity discontinuities on Thompson Glacier are small (several cm d^{-1}), spatial
581 smoothing of the speckle tracking results, as is commonly done to reduce errors, obscures the discontinuities.
582 Instead, we analyze the possible causes of speckle tracking errors and find that false matches often occur
583 when speckle tracking locks-on to high intensity pixels, which in SAR images of glaciers, are often structural
584 features such as crevasses or stream channels. To improve SAR speckle tracking performance, we use a
585 SAR simulator capable of generating SLC pairs with a user defined motion field to study optimum intensity
586 rescaling as a pre-conditioning step. The intensity-rescaled speckle tracking is then used to measure the
587 motion of the Expedition Fjord area glaciers.

588 The measured glacier speeds compare well (MAE of 0.52 cm d^{-1}) to annual speeds from NASA ITS_LIVE
589 data, a lower resolution global glacier motion dataset. Interferograms indicate that cross-channel discon-
590 tinuous motion is occurring along three supraglacial channels on Thompson Glacier. However, only at the
591 Astro Channel is the magnitude of the velocity discontinuity large enough to be resolved by the speckle

Corti and others:

592 tracking results, indicating that the discontinuity at the other two channels is $\lesssim 0.5 \text{ cm d}^{-1}$. The remote
593 sensing observations show an uncommon form of discontinuous glacier motion characterized by ice on
594 the central (west) side of the Astro Channel flowing approximately 30% (1 cm d^{-1}) faster than the ice
595 immediately across the $\sim 3 \text{ m}$ wide channel.

596 A cross-sectional ice-flow model is used to investigate the physical causes of this discontinuous motion.
597 The finite-element ice-flow model uses a domain inspired by Thompson Glacier that includes a surface
598 channel similar to the Astro Channel. The modeling shows that discontinuous glacier motion of the form
599 and magnitude observed across the Astro Channel can occur, without ice fracture and under a wide variety
600 of plausible channel depths and thermal structures, including in temperate glaciers.

601 We also use the ice-flow model to investigate the sensitivity of the velocity discontinuity to various
602 model parameters. Channel depth is the primary control on the velocity discontinuity, but low surface
603 temperatures and high in-channel temperatures, caused in the real world by water flow within the channel,
604 also contribute to larger cross-channel velocity discontinuities. Again, the modeling demonstrates that
605 specific or unusual thermal structures are not necessary to cause cross-channel discontinuous motion,
606 implying that the rarity of this form of motion is instead a result of the channel geometry. Namely,
607 the channel must be deep, straight, flow-following and long, and located in areas of high lateral shear
608 stress. We speculate that channels conducive to discontinuous motion form and persist preferentially on
609 polythermal glaciers, particularly in the presence of glacier confluences and their associated ice-marginal
610 lakes.

611 SUPPLEMENTARY MATERIAL

612 The supplementary material for this article can be found at <https://doi.org/xxxxxx>

613 ACKNOWLEDGEMENTS

614 SFU, NSERC, CSA and MDA contributed funding for this study. We thank MDA for their support in
615 obtaining RADARSAT-2 data and acknowledge J Eppler for helpful discussions on creating simulated
616 SAR images. We are grateful to L. Thomson for providing advice, photographs and study-site specific
617 knowledge. Finally, we would like to thank B. Minchew and a second anonymous reviewer for their
618 thorough and insightful comments.

619 **AUTHOR CONTRIBUTIONS**

620 BR broadly conceived of the remote sensing portion of this study with specifics determined by GC. GC
621 conceived of the glacier modeling portion with input from GF and BR. GC carried out both remote sensing
622 and ice-flow analysis and modeling with with guidance from BR and GF. GC led manuscript preparation
623 with advice and editing from BR and GF.

624 **REFERENCES**

- 625 Adams CJ, Iverson NR, Helanow C, Zoet LK and Bate CE (2021) Softening of temperate ice by interstitial water.
626 *Frontiers in Earth Science*, **9**, 702761 (doi: 10.3389/feart.2021.702761)
- 627 Amundson JM, Truffer M and Lüthi MP (2006) Time-dependent basal stress conditions beneath Black Rapids
628 Glacier, Alaska, USA, inferred from measurements of ice deformation and surface motion. *Journal of Glaciology*,
629 **52**(178), 347–357 (doi: 10.3189/172756506781828593)
- 630 Armstrong W, Anderson R, Allen J and Rajaram H (2016) Modeling the WorldView-derived seasonal velocity
631 evolution of Kennicott Glacier, Alaska. *Journal of Glaciology*, **62**(234), 763–777 (doi: 10.1017/jog.2016.66)
- 632 Bamler R and Eineder M (2005) Accuracy of differential shift estimation by correlation and split-bandwidth inter-
633 ferometry for wideband and delta-k SAR systems. *IEEE Geoscience and Remote Sensing Letters*, **2**(2), 151–155
634 (doi: 10.1109/lgrs.2004.843203)
- 635 Bamler R, Eineder M, Adam N, Zhu X and Gernhardt S (2009) Interferometric potential of high resolution spaceborne
636 SAR. *Photogrammetrie-Fernerkundung-Geoinformation*, **5**, 407–419 (doi: 10.1127/1432-8364/2009/0029)
- 637 Bingham RG, Nienow PW and Sharp M (2003) Intra-annual and intra-seasonal flow dynamics of a High Arctic
638 polythermal valley glacier. *Annals of Glaciology*, **37**, 181–188 (doi: 10.3189/172756403781815762)
- 639 Bingham RG, Nienow PW, Sharp M and Copland L (2006) Hydrology and dynamics of a polythermal (mostly
640 cold) High Arctic glacier. *Earth Surface Processes and Landforms: The Journal of the British Geomorphological
641 Research Group*, **31**(12), 1463–1479 (doi: 10.1002/esp.1374)
- 642 Blatter H (1987) Stagnant ice at the bed of White Glacier, Axel Heiberg Island. N.W.T, Canada. *Annals of Glaciology*,
643 **9**, 35–38 (doi: 10.1017/s0260305500000343)
- 644 Closson D and Milisavljevic N (2017) InSAR coherence and intensity changes detection. In *Mine Action - The
645 Research Experience of the Royal Military Academy of Belgium*, InTech (doi: 10.5772/65779)

Corti and others:

- 646 Cogley J, Adams WP and Ecclestone M (2011) Half a century of measurements of glaciers on Axel Heiberg Island,
647 Nunavut, Canada. *Arctic*, 371–375 (doi: 10.14430/arctic4127)
- 648 Cogley JG, Adams W, Ecclestone M, Jung-Rothenhäusler F and Ommanney C (1996) Mass balance of white
649 glacier, Axel Heiberg Island, N.W.T., Canada, 1960–91. *Journal of Glaciology*, **42**(142), 548–563 (doi: 10.3189/
650 s0022143000003531)
- 651 Colgan W, Rajaram H, Abdalati W, McCutchan C, Mottram R, Moussavi MS and Grigsby S (2016) Glacier crevasses:
652 Observations, models, and mass balance implications: Glacier crevasses. *Reviews of Geophysics*, **54**(1), 119–161
653 (doi: 10.1002/2015rg000504)
- 654 Cook SJ, Swift DA, Kirkbride MP, Knight PG and Waller RI (2020) The empirical basis for modelling glacial erosion
655 rates. *Nature communications*, **11**(1), 759
- 656 Cuffey KM and Paterson WSB (2010) *The physics of glaciers*. Academic Press
- 657 Cumming IG and Zhang J (1999) Measuring the 3-D flow of the Lowell Glacier with InSAR. *Proceedings of ESA*
658 *Fringe*, **99**
- 659 De Zan F (2014) Accuracy of incoherent speckle tracking for circular gaussian signals. *IEEE Geoscience and Remote*
660 *Sensing Letters*, **11**(1), 264–267 (doi: 10.1109/lgrs.2013.2255259)
- 661 Duval P (1977) The role of the water content on the creep rate of polycrystalline ice. *Proc. Grenoble Symposium*,
662 *1975*, **118**, 29–33
- 663 Enderlin EM, Howat IM and Vieli A (2013) The sensitivity of flowline models of tidewater glaciers to parameter
664 uncertainty. *The Cryosphere*, **7**(5), 1579–1590 (doi: <https://doi.org/10.5194/tc-7-1579-2013>)
- 665 Esri (2022) ‘World Imagery’ [basemap]. 15 m scale. Available at [www.arcgis.com/home/item.html?id=](http://www.arcgis.com/home/item.html?id=10df2279f9684e4a9f6a7f08febac2a9)
666 [10df2279f9684e4a9f6a7f08febac2a9](http://www.arcgis.com/home/item.html?id=10df2279f9684e4a9f6a7f08febac2a9) (September 23, 2022)
- 667 Eyles N and Rogerson R (1977) Glacier movement, ice structures, and medial moraine form at a glacier confluence,
668 Berendon Glacier, British Columbia, Canada. *Canadian Journal of Earth Sciences*, **14**(12), 2807–2816
- 669 Faillettaz J, Funk M and Vincent C (2015) Avalanching glacier instabilities: Review on processes and early warning
670 perspectives. *Reviews of Geophysics*, **53**(2), 203–224
- 671 Farinotti D, Huss M, Fürst JJ, Landmann J, Machguth H, Maussion F and Pandit A (2019) A consensus estimate
672 for the ice thickness distribution of all glaciers on Earth. *Nature Geoscience*, **12**(3), 168–173 (doi: 10.1038/
673 s41561-019-0300-3)

- 674 Fatland DR and Lingle CS (2002) InSAR observations of the 1993–95 Bering Glacier (Alaska, USA) surge and a
675 surge hypothesis. *Journal of Glaciology*, **48**(162), 439–451 (doi: 10.3189/172756502781831296)
- 676 Ferguson R (1973) Sinuosity of supraglacial streams. *Geological Society of America Bulletin*, **84**(1), 251–256 (doi:
677 10.1130/0016-7606(1973)84<251:soss>2.0.co;2)
- 678 Gardner AS, Moholdt G, Scambos T, Fahnestock M, Ligtenberg S, den Broeke MV and Nilsson J (2018) Increased
679 west antarctic and unchanged east antarctic ice discharge over the last 7 years. *The Cryosphere*, **12**(2), 521–547
680 (doi: 10.5194/tc-12-521-2018)
- 681 Gardner AS, Fahnestock M and Scambos T (2022) Measures its_live regional glacier and ice sheet surface velocities,
682 version 1 (doi: 10.5067/6II6VW8LLWJ7)
- 683 Geuzaine C and Remacle JF (2009) Gmsh: A 3-d finite element mesh generator with built-in pre-and post-processing
684 facilities. *International journal for numerical methods in engineering*, **79**(11), 1309–1331 (doi: 10.1002/nme.2579)
- 685 Glasser NF and Gudmundsson G (2012) Longitudinal surface structures (flowstripes) on Antarctic glaciers. *The
686 Cryosphere*, **6**(2), 383–391 (doi: 10.5194/tc-6-383-2012)
- 687 Goldstein RM, Engelhardt H, Kamb B and Frolich RM (1993) Satellite radar interferometry for monitoring ice sheet
688 motion: application to an Antarctic ice stream. *Science*, **262**(5139), 1525–1530 (doi: 10.1126/science.262.5139.
689 1525)
- 690 Gray AL, Mattar K, Vachon P, Bindschadler R, Jezek K, Forster R and Crawford J (1998) InSAR results from the
691 RADARSAT Antarctic Mapping Mission data: estimation of glacier motion using a simple registration procedure.
692 In *IGARSS'98. Sensing and Managing the Environment. 1998 IEEE International Geoscience and Remote Sensing.
693 Symposium Proceedings.(Cat. No. 98CH36174)*, volume 3, 1638–1640, IEEE (doi: 10.4095/219342)
- 694 Gray AL, Short NH, Mattar K and Jezek K (2001) Velocities and flux of the Filchner ice shelf and its tributaries
695 determined from speckle tracking interferometry. *Canadian Journal of Remote Sensing*, **27**(3), 193–206 (doi: 10.
696 4095/219822)
- 697 Hambrey MJ (1977) Supraglacial drainage and its relationship to structure, with particular reference to charles
698 rabots bre, okstindan, norway. *Norsk Geografisk Tidsskrift - Norwegian Journal of Geography*, **31**(2), 69–77 (doi:
699 10.1080/00291957708545319)
- 700 Hambrey MJ and Müller F (1978) Structures and ice deformation in the White Glacier, Axel Heiberg Island, North-
701 west Territories, Canada. *Journal of Glaciology*, **20**(82), 41–66 (doi: 10.1017/s0022143000021213)

Corti and others:

- 702 Ignatenko V, Laurila P, Radius A, Lamentowski L, Antropov O and Muff D (2020) ICEYE microsatellite SAR
703 constellation status update: Evaluation of first commercial imaging modes. In *IGARSS 2020-2020 IEEE Interna-*
704 *tional Geoscience and Remote Sensing Symposium*, 3581–3584, IEEE (doi: [https://doi.org/10.1109/igarss39084.](https://doi.org/10.1109/igarss39084.2020.9324531)
705 [2020.9324531](https://doi.org/10.1109/igarss39084.2020.9324531))
- 706 Irvine-Fynn TD, Hodson AJ, Moorman BJ, Vatne G and Hubbard AL (2011) Polythermal glacier hydrology: a
707 review. *Reviews of Geophysics*, **49**(4) (doi: [10.1029/2010rg000350](https://doi.org/10.1029/2010rg000350))
- 708 Isenko E, Naruse R and Mavlyudov B (2005) Water temperature in englacial and supraglacial channels: Change
709 along the flow and contribution to ice melting on the channel wall. *Cold regions science and technology*, **42**(1),
710 53–62 (doi: [10.1016/j.coldregions.2004.12.003](https://doi.org/10.1016/j.coldregions.2004.12.003))
- 711 Jacka T and Budd W (1989) Isotropic and anisotropic flow relations for ice dynamics. *Annals of glaciology*, **12**, 81–84
- 712 Joughin I (2002) Ice-sheet velocity mapping: a combined interferometric and speckle-tracking approach. *Annals of*
713 *Glaciology*, **34**, 195–201 (doi: [10.3189/172756402781817978](https://doi.org/10.3189/172756402781817978))
- 714 Joughin I, Smith BE and Abdalati W (2011) Glaciological advances made with interferometric synthetic aperture
715 radar. *Journal of Glaciology*, **56**(200), 1026–1042 (doi: [10.3189/002214311796406158](https://doi.org/10.3189/002214311796406158))
- 716 Joughin I, Smith BE and Howat IM (2018) A complete map of Greenland ice velocity derived from satellite data
717 collected over 20 years. *Journal of Glaciology*, **64**(243), 1–11 (doi: [10.1017/jog.2017.73](https://doi.org/10.1017/jog.2017.73))
- 718 Jun L, Jacka T and Budd W (1996) Deformation rates in combined compression and shear for ice which is initially
719 isotropic and after the development of strong anisotropy. *Annals of Glaciology*, **23**, 247–252 (doi: [https://doi.org/](https://doi.org/10.1016/0148-9062(85)90267-0)
720 [10.1016/0148-9062\(85\)90267-0](https://doi.org/10.1016/0148-9062(85)90267-0))
- 721 Kaiser HF and Dickman K (1962) Sample and population score matrices and sample correlation matrices from an
722 arbitrary population correlation matrix. *Psychometrika*, **27**(2), 179–182 (doi: [10.1007/bf02289635](https://doi.org/10.1007/bf02289635))
- 723 Kobayashi T, Morishita Y and Yurai H (2018) SAR-revealed slip partitioning on a bending fault plane for the 2014
724 northern Nagano earthquake at the northern Itoigawa–Shizuoka tectonic line. *Tectonophysics*, **733**, 85–99 (doi:
725 [10.1016/j.tecto.2017.12.001](https://doi.org/10.1016/j.tecto.2017.12.001))
- 726 Lee JS (1983) A simple speckle smoothing algorithm for synthetic aperture radar images. *IEEE Transactions on*
727 *Systems, Man, and Cybernetics*, (1), 85–89 (doi: [10.1109/tsmc.1983.6313036](https://doi.org/10.1109/tsmc.1983.6313036))
- 728 Lei Y, Gardner A and Agram P (2021) Autonomous repeat image feature tracking (autoRIFT) and its application
729 for tracking ice displacement. *Remote Sensing*, **13**(4), 749 (doi: <https://doi.org/10.3390/rs13040749>)
- 730 Maag HU (1963) Marginal drainage and glacier-dammed lakes

- 731 Magnard C, Werner C and Wegmuller U (2017) GAMMA Technical Report: Offset estimation programs update.
732 Technical report
- 733 MDA (2018) RADARSAT-2 product description. Technical report, Available at [https://earth.esa.int/eogateway/documents/20142/0/Radarsat-2-Product-description.pdf/](https://earth.esa.int/eogateway/documents/20142/0/Radarsat-2-Product-description.pdf/f2783c7b-6a22-cbe4-f4c1-6992f9926dca)
734 [f2783c7b-6a22-cbe4-f4c1-6992f9926dca](https://earth.esa.int/eogateway/documents/20142/0/Radarsat-2-Product-description.pdf/f2783c7b-6a22-cbe4-f4c1-6992f9926dca)
735
- 736 Michel R and Rignot E (1999) Flow of Glaciar Moreno, Argentina, from repeat-pass Shuttle Imaging Radar images:
737 comparison of the phase correlation method with radar interferometry. *Journal of Glaciology*, **45**(149), 93–100
738 (doi: 10.3189/s0022143000003075)
- 739 Millan R, Mouginot J, Derkacheva A, Rignot E, Milillo P, Ciraci E, Dini L and Bjørk A (2022a) Ongoing grounding
740 line retreat and fracturing initiated at the Petermann Glacier ice shelf, Greenland, after 2016. *The Cryosphere*,
741 **16**(7), 3021–3031 (doi: 10.5194/tc-16-3021-2022)
- 742 Millan R, Mouginot J, Rabatel A and Morlighem M (2022b) Ice velocity and thickness of the world's glaciers. *Nature*
743 *Geoscience*, **15**(2), 124–129 (doi: 10.1038/s41561-021-00885-z)
- 744 Minchew B, Simons M, Hensley S, Björnsson H and Pálsson F (2015) Early melt season velocity fields of Langjökull
745 and Hofsjökull, central Iceland. *Journal of Glaciology*, **61**(226), 253–266 (doi: 10.3189/2015jog14j023)
- 746 Minchew B, Simons M, Björnsson H, Pálsson F, Morlighem M, Seroussi H, Larour E and Hensley S (2016) Plastic
747 bed beneath Hofsjökull ice cap, central Iceland, and the sensitivity of ice flow to surface meltwater flux. *Journal*
748 *of Glaciology*, **62**(231), 147–158 (doi: 10.1017/jog.2016.26)
- 749 Mohammadimanesh F, Salehi B, Mahdianpari M, Brisco B and Motagh M (2018) Multi-temporal, multi-frequency,
750 and multi-polarization coherence and SAR backscatter analysis of wetlands. *ISPRS Journal of Photogrammetry*
751 *and Remote Sensing*, **142**, 78–93 (doi: 10.1016/j.isprsjprs.2018.05.009)
- 752 Monz ME, Hudleston PJ, Cook SJ, Zimmerman T and Leng MJ (2022) Thrust faulting in glaciers? re-examination
753 of debris bands near the margin of Storglaciären, Sweden. *Boreas*, **51**(1), 78–99 (doi: 10.1111/bor.12549)
- 754 Moore PL, Iverson NR and Cohen D (2010) Conditions for thrust faulting in a glacier. *Journal of Geophysical*
755 *Research: Earth Surface*, **115**(F2) (doi: 10.1029/2009jf001307)
- 756 Moreira A, Prats-Iraola P, Younis M, Krieger G, Hajnsek I and Papathanassiou KP (2013) A tutorial on synthetic
757 aperture radar. *IEEE Geoscience and Remote Sensing Magazine*, **1**(1), 6–43 (doi: 10.1109/mgrs.2013.2248301)
- 758 Morena L, James K and Beck J (2004) An introduction to the RADARSAT-2 mission. *Canadian Journal of Remote*
759 *Sensing*, **30**(3), 221–234 (doi: 10.5589/m04-004)

Corti and others:

- 760 Müller F (1962) Zonation in the accumulation area of the glaciers of Axel Heiberg Island, N.W.T., Canada. *Journal*
761 *of Glaciology*, **4**(33), 302–311, ISSN 0022-1430, 1727-5652 (doi: 10.3189/s0022143000027623)
- 762 Nagler T, Rott H, Hetzenecker M, Scharrer K, Magnússon E, Floricioiu D and Notarnicola C (2012) Retrieval of
763 3D-glacier movement by high resolution X-band SAR data. In *2012 IEEE International Geoscience and Remote*
764 *Sensing Symposium*, 3233–3236, IEEE (doi: 10.1109/igarss.2012.6350735)
- 765 Nye JF (1965) The flow of a glacier in a channel of rectangular, elliptic or parabolic cross-section. *Journal of glaciology*,
766 **5**(41), 661–690 (doi: 10.3189/s0022143000018670)
- 767 Pepe A and Calò F (2017) A review of interferometric synthetic aperture RADAR (InSAR) multi-track approaches
768 for the retrieval of Earth's surface displacements. *Applied Sciences*, **7**(12), 1264 (doi: 10.3390/app7121264)
- 769 Porter C, Morin P, Howat I, Noh MJ, Bates B, Peterman K, Keeseey S, Schlenk M, Gardiner J, Tomko K, Willis M,
770 Kelleher C, Cloutier M, Husby E, Foga S, Nakamura H, Platson M, Wethington J Michael, Williamson C, Bauer
771 G, Enos J, Arnold G, Kramer W, Becker P, Doshi A, D'Souza C, Cummins P, Laurier F and Bojesen M (2018)
772 ArcticDEM (doi: 10.7910/DVN/OHHUKH)
- 773 Rabus B and Echelmeyer KA (1997) The flow of a polythermal glacier: McCall Glacier, Alaska, U.S.A. *Journal of*
774 *Glaciology*, **43**(145), 522–536 (doi: 10.3189/s0022143000035139)
- 775 Rabus BT and Lang O (2002) On the representation of ice-shelf grounding zones in SAR interferograms. *Journal of*
776 *Glaciology*, **48**(162), 345–356 (doi: 10.3189/172756502781831197)
- 777 Rathgeber F, Ham DA, Mitchell L, Lange M, Luporini F, McRae AT, Bercea GT, Markall GR and Kelly PH (2016)
778 Firedrake: automating the finite element method by composing abstractions. *ACM Transactions on Mathematical*
779 *Software (TOMS)*, **43**(3), 1–27 (doi: 10.1145/2998441)
- 780 Rignot E (1996) Tidal motion, ice velocity and melt rate of Petermann Gletscher, Greenland, measured from radar
781 interferometry. *Journal of Glaciology*, **42**(142), 476–485 (doi: 10.3189/s0022143000003464)
- 782 Rignot E (1998) Fast recession of a West Antarctic glacier. *Science*, **281**(5376), 549–551 (doi: 10.1126/science.281.
783 5376.549)
- 784 Shapero DR, Badgeley JA, Hoffman AO and Joughin I (2021) icepack: A new glacier flow modeling package in
785 python, version 1.0. *Geoscientific Model Development*, **14**(7), 4593–4616 (doi: 10.5194/gmd-14-4593-2021)
- 786 St Germain SL and Moorman BJ (2019) Long-term observations of supraglacial streams on an Arctic glacier. *Journal*
787 *of Glaciology*, **65**(254), 900–911 (doi: 10.1017/jog.2019.60)

- 788 Thomson LI and Copland L (2017) Multi-decadal reduction in glacier velocities and mechanisms driving deceleration
789 at polythermal White Glacier, Arctic Canada. *Journal of Glaciology*, **63**(239), 450–463 (doi: 10.1017/jog.2017.3)
- 790 Thomson LI, Zemp M, Copland L, Cogley J and Ecclestone MA (2017) Comparison of geodetic and glaciological mass
791 budgets for White Glacier, Axel Heiberg Island, Canada. *Journal of Glaciology*, **63**(237), 55–66, ISSN 0022-1430,
792 1727-5652 (doi: 10.1017/jog.2016.112)
- 793 Van Wychen W, Copland L, Jiskoot H, Gray AL, Sharp M and Burgess D (2018) Surface velocities of glaciers in
794 western Canada from speckle-tracking of ALOS PALSAR and RADARSAT-2 data. *Canadian Journal of Remote
795 Sensing*, **44**(1), 57–66 (doi: 10.1080/07038992.2018.1433529)
- 796 Wang Q, Fan J, Zhou W, Tong L, Guo Z, Liu G, Yuan W, Sousa JJ and Perski Z (2019) 3D surface velocity retrieval
797 of mountain glacier using an offset tracking technique applied to ascending and descending SAR constellation data:
798 a case study of the Yiga Glacier. *International Journal of Digital Earth*, **12**(6), 614–624 (doi: 10.1080/17538947.
799 2018.1470690)
- 800 Weertman J (1957) On the sliding of glaciers. *Journal of glaciology*, **3**(21), 33–38 (doi: 10.3189/s0022143000024709)
- 801 Williams JJ, Gourmelen N and Nienow P (2021) Complex multi-decadal ice dynamical change inland of marine-
802 terminating glaciers on the Greenland Ice Sheet. *Journal of Glaciology*, **67**(265), 833–846 (doi: [https://doi.org/
803 10.1017/jog.2021.31](https://doi.org/10.1017/jog.2021.31))
- 804 Wilson N, Flowers G and Mingo L (2013) Comparison of thermal structure and evolution between neighboring
805 subarctic glaciers. *Journal of Geophysical Research: Earth Surface*, **118**(3), 1443–1459 (doi: 10.1002/jgrf.20096)
- 806 Xie H, Pierce LE and Ulaby FT (2002) Statistical properties of logarithmically transformed speckle. *IEEE transactions
807 on geoscience and remote sensing*, **40**(3), 721–727 (doi: 10.1109/tgrs.2002.1000333)
- 808 Yang Y, Li Z, Huang L, Tian B and Chen Q (2016) Extraction of glacier outlines and water-eroded stripes using
809 high-resolution SAR imagery. *International Journal of Remote Sensing*, **37**(5), 1016–1034 (doi: [https://doi.org/
810 10.1080/01431161.2016.1145365](https://doi.org/10.1080/01431161.2016.1145365))
- 811 Yoo JC and Han TH (2009) Fast normalized cross-correlation. *Circuits, Systems and Signal Processing*, **28**(6), 819–
812 843 (doi: 10.1007/s00034-009-9130-7)
- 813 Yu H, Lan Y, Yuan Z, Xu J and Lee H (2019) Phase unwrapping in InSAR: A review. *IEEE Geoscience and Remote
814 Sensing Magazine*, **7**(1), 40–58 (doi: 10.1109/MGRS.2018.2873644)